

RESEARCH ARTICLE | JANUARY 12 2023

# Data-driven turbulence model for unsteady cavitating flow


Special Collection: [Cavitation](#)

Zhen Zhang (张珍) ; Jingzhu Wang (王静竹) ; Renfang Huang (黄仁芳) ; Rundi Qiu (丘润荻); Xuesen Chu (褚学森); Shuran Ye (叶舒然); Yiwei Wang (王一伟)  ; Qingkuan Liu (刘庆宽) 




*Physics of Fluids* 35, 015134 (2023)

<https://doi.org/10.1063/5.0134992>



**APL Machine Learning**  
2023 Papers with Best Practices in Data Sharing and Comprehensive Background  
[Read Now](#)



# Data-driven turbulence model for unsteady cavitating flow

Cite as: Phys. Fluids **35**, 015134 (2023); doi: 10.1063/5.0134992

Submitted: 15 November 2022 · Accepted: 23 December 2022 ·

Published Online: 12 January 2023



View Online



Export Citation



CrossMark

Zhen Zhang (张珍),<sup>1,2,3</sup>  Jingzhu Wang (王静竹),<sup>4</sup>  Renfang Huang (黄仁芳),<sup>4</sup>  Rundi Qiu (丘润荻),<sup>4,5</sup>  
Xuesen Chu (褚学森),<sup>6,7</sup>  Shuran Ye (叶舒然),<sup>4,8</sup>  Yiwei Wang (王一伟),<sup>4,5,8,a)</sup>  and Qingkuan Liu (刘庆宽)<sup>1,2,3</sup> 

## AFFILIATIONS

<sup>1</sup>State Key Laboratory of Mechanical Behavior and System Safety of Traffic Engineering Structures, Shijiazhuang Tiedao University, Shijiazhuang 050043, China

<sup>2</sup>Key Laboratory of Roads and Railway Engineering Safety Control (Shijiazhuang Tiedao University), Ministry of Education, Shijiazhuang 050043, China

<sup>3</sup>Innovation Center for Wind Engineering and Wind Energy Technology of Hebei Province, Shijiazhuang 050043, China

<sup>4</sup>Key Laboratory for Mechanics in Fluid Solid Coupling Systems, Institute of Mechanics, Chinese Academy of Sciences, Beijing 100190, China

<sup>5</sup>School of Future Technology, University of Chinese Academy of Sciences, Beijing 100049, China

<sup>6</sup>China Ship Scientific Research Center, Wuxi 214082, China

<sup>7</sup>Taihu Laboratory of Deepsea Technological Science, Wuxi 214000, China

<sup>8</sup>School of Engineering Science, University of Chinese Academy of Sciences, Beijing 100049, China

**Note:** This paper is part of the special topic, Cavitation.

<sup>a)</sup>Author to whom correspondence should be addressed: [wangyw@imech.ac.cn](mailto:wangyw@imech.ac.cn)

## ABSTRACT

Unsteady Reynolds-averaged Navier–Stokes (URANS) equations have been widely used in engineering fields to investigate cavitating flow owing to their low computational cost and excellent robustness. However, it is challenging to accurately obtain the unsteady characteristics of flow owing to cavitation-induced phase transitions. In this study, we propose an implicit data-driven URANS (DD-URANS) framework to analyze the unsteady characteristics of cavitating flow. In the DD-URANS framework, a basic computational model is developed by introducing a cavitation-induced phase transition into the equations of Reynolds stress. To improve the computational accuracy and generalization performance of the basic model, the linear and nonlinear parts of the anisotropic Reynolds stress are predicted through implicit and explicit methods, respectively. A data fusion approach, allowing the input and output of characterized parameters at multiple time points, is presented to obtain the unsteady characteristics of the cavitating flow. The DD-URANS model is trained using the numerical results obtained via large-eddy simulation. The training data consist of two parts: (i) the results obtained at cavitation numbers of 2.0, 2.2, and 2.7 for a Venturi flow, and (ii) those obtained at cavitation numbers of 0.8 and 1.5 for a National Advisory Committee for Aeronautics (NACA) 66 hydrofoil. The DD-URANS model is used to predict the cavitating flow at cavitation numbers of 2.5 for a Venturi flow and 0.8 for a Clark-Y hydrofoil. It is found that the DD-URANS model is superior to the baseline URANS model in predicting the instantaneous periodic shedding of a cavity and the mean flow fields.

Published under an exclusive license by AIP Publishing. <https://doi.org/10.1063/5.0134992>

## I. INTRODUCTION

Studies on cavitating flow have received increasing attention because the performance of equipment and vehicles is affected by its unsteady development. A phase transition occurs and forms a cavity when the local fluid pressure decreases rapidly to the saturated vapor pressure; this process is called cavitation. Cavitation is always accompanied by vibration, noise, and erosion.<sup>1,2</sup> In addition, the load fluctuation

caused by the periodic cavity shedding and the pressure pulsation caused by the bubble collapse are also easy to cause the damage of the structure.<sup>3</sup> Cavitation must be prevented for many applications,<sup>4</sup> and thus, it is necessary to analyze unsteady cavitating flow to optimize and design equipment and vehicles for engineering applications.<sup>5,6</sup>

The cavitating flow is closely related to the turbulent flow, and the cavitation–vortex interaction impacts the cavity evolution

profoundly.<sup>7</sup> In the cavitation inception, the generation of Reynolds stress in the turbulent boundary layer directly affects the burst process of near-wall coherent structures.<sup>8</sup> Bappy *et al.*<sup>2</sup> studied the pressure statistics of gas nuclei in homogeneous isotropic turbulence and its application in cavitation inception. The results have a significant impact on the modeling of cavitation inception. With the generation and development of cavitation, the formation of vortex motion will strengthen the turbulence intensity of the flow, making the interaction mechanism between turbulence and cavitation more complex.<sup>9</sup>

The cavitating motion plays a significant role in the turbulence velocity fluctuation and turbulence anisotropy; therefore, it is challenging to precisely simulate the unsteady characteristics of cavitating flow.<sup>10–13</sup> Large-eddy simulation (LES) is one of the most effective approaches for analyzing multiscale vortices and directly solves large-scale vortices by filtering while modeling small-scale vortices. Wang and Ostoja-Starzewski<sup>14</sup> used the LES approach to analyze the National Advisory Committee for Aeronautics (NACA) 0015 hydrofoil and obtained details regarding the shedding of the cavity. Ji *et al.*<sup>15</sup> obtained the evolution laws of a cavity during the oscillating process by using the LES approach, which results were in good agreement with the experimental results. They also found that the development and collapse of the cavity complicate the numerical computations. Considering the influence of the unresolved pressure fluctuations at the sub-grid scale (SGS) level computed by LES on cavitation inception prediction, Bappy *et al.*<sup>4</sup> proposed a SGS model of cavitation inception, which took into account the unresolved SGS pressure fluctuations and successfully predicted the initial pressure and cavitation rate in the flow. Yu *et al.*<sup>7</sup> utilized the LES approach to predict the cavitating flow around a Delft Twist-11 hydrofoil. They refined the nodes near the Delft Twist-11 hydrofoil surface to guarantee the capacity to capture the cavitating flow details. It is found that the numerical results showed a reasonable agreement with the experimental data, and the cavitating motion plays a significant role in the turbulence anisotropy. Wu, Wang, and Huang<sup>16</sup> investigated the influence of mesh resolution on the results using the LES approach with two sets of grids. In this work, the numerical simulation results based on the coarse grid showed that the predicted cavity length and cavity shedding periodic were different from the experimental results. Considering the influence of cavity length and velocity of reentry jet on the shedding frequency, and the sensitivity of the reentry jet in spanwise direction to the pressure gradient and spanwise resolution of the mesh, the grid setting was further optimized. They captured the reentry jet in the spanwise direction by setting more spanwise nodes and then predicted the cavity length, cavity shedding period, and cavitation mode, which in good agreement with the experimental results. Yu, Feng, and Tang<sup>17</sup> used the refined meshes optimized in the spanwise to capture the intrinsic vortex structure around a mini cascade and revealed the interaction between vortex dynamics and turbulence–cavitation. As mentioned above, a high grid resolution and large computational cost are required to simulate cavitating flow using the LES approach, and this limits the application of the LES approach in engineering fields.<sup>18</sup>

Unsteady Reynolds-averaged Navier–Stokes (URANS) equations have been widely used in engineering fields to investigate cavitating flow owing to their low computational cost and excellent robustness. In the traditional URANS approach, the standard  $k - \varepsilon$  model treats turbulent viscosity as a function of the turbulent kinetic energy and dissipation rate and is used to analyze the development of

turbulence.<sup>19</sup> This approach shows better computing stability and independence in terms of computing resources compared to LES.<sup>20</sup> However, this method overestimates the turbulent viscosity,<sup>18,21–23</sup> thus, the details of unsteady behaviors cannot be simulated accurately in a complex cavitating flow.<sup>24–26</sup> To avoid the viscosity over-prediction observed using the traditional URANS model, Coutier-Delgosha, Patella, and Reboud<sup>27</sup> and Li *et al.*<sup>28</sup> proposed a density-based URANS model by introducing a mixing density function into the traditional turbulence viscosity. Wang *et al.*<sup>29</sup> carried out numerical simulations to analyze a cloud cavitating flow in a revolving body. Their results showed that the modified URANS roughly described the shapes of the cavity compared to the results obtained using the LES approach. Although the modified URANS model improves the prediction performance in cavitating flow, the unsteady characteristics of this flow are not accurately obtained relative to the LES approach. However, the URANS turbulence model still plays an important role in engineering applications.<sup>30</sup> Consequently, novel turbulence models should be developed to further enhance the prediction performance of the URANS model in cavitating flow.

Recently, data-driven (DD) techniques in machine learning algorithms have been widely used in turbulence closure modeling to enhance predictive capabilities and computational accuracy.<sup>31–41</sup> Among them, the tree-based methods,<sup>42</sup> support vector machine Ling and Templeton,<sup>43</sup> and artificial neural network<sup>44,45</sup> are the main data-driven technologies. In the turbulence modeling framework, regression functions are obtained via the data-driven technique based on datasets and are used to develop Reynolds stress closures. The traditional RANS model is modified based on the predicted Reynolds stress closure, and this modification is based on the certain fundamental physical principles and closure tenets incumbent.<sup>31</sup> Ling *et al.*<sup>45</sup> proposed a specific network structure based on the framework of a higher-order eddy-viscosity model and used base tensors to ensure Galileo invariance. Subsequently, the strategy used to ensure Galileo invariance was applied to different types of flows such as channel flows, back steps, and periodic mountain flows.<sup>46–51</sup> The above-mentioned studies showed that data-driven RANS models are superior to the traditional RANS model. In these studies, the Reynolds stress was predicted explicitly, while the other terms in the momentum and transport equations remained unchanged.

However, the explicit treatment of the Reynolds stress led to ill-conditioning of the RANS equations, inducing a low prediction accuracy of the posterior flow. Wu, Xiao, and Paterson<sup>52</sup> proposed an implicit treatment method based on physical information. In this method, the linear and nonlinear parts of the Reynolds stress are trained separately to improve the prediction accuracy. Wu *et al.*<sup>53</sup> introduced a local condition number function to evaluate the conditional characteristics of the turbulence model. The local condition number was used to quantitatively explain the improvement in the implicit treatment of Reynolds stress. Zhang *et al.*<sup>54</sup> developed a semi-implicit treatment of an anisotropy discrepancy model of Reynolds stress based on a higher-order tensor basis. Their results showed that the prediction accuracy in the posterior flow was improved significantly.

As mentioned above, while steady flows have been predicted precisely via the data-driven RANS model, studies on the prediction of a cavitating flow have rarely been carried out owing to a variety of complex phenomena such as turbulence, phase transition, and unsteady characteristics. In the present study, an implicit data-driven URANS

(DD-URANS) framework is proposed to analyze the unsteady characteristics of cloud cavitating flow. In this framework, the effects of cavitation are considered by introducing the rate of phase transition into the URANS equations. The anisotropic Reynolds stresses are decomposed into linear and nonlinear components, which are trained using implicit and explicit treatment methods, respectively. Training data are obtained using the LES wall-adapting local-eddy viscosity (WALE) model Nicoud and Ducros.<sup>55</sup> Moreover, to improve the calculation of the unsteady characteristics of cavitating flow, we developed a multi-time data fusion method using a temporal distribution to construct the dataset. Our numerical results indicate that the DD-URANS model is superior to the traditional URANS model for predicting unsteady characteristics in a cavitating flow. Furthermore, the developed DD-URANS exhibited excellent generalization ability. The structure of the present study is as follows: Sec. II describes the implicit DD-URANS model and training dataset. Section III discusses the prediction results of the DD-URANS model. The findings of this study are finally summarized in Sec. IV.

## II. METHODOLOGY

In the typical cloud cavitation regime, the development process of the cavity is periodic, and the reentry jet formed by the attached cavity tail is the main reason for the cloud cavity shedding.<sup>25</sup> Shedding by the mechanism of reentry flow is regarded as a three-part process involving the development of the reentry flow, cavity shedding, and cavity growth, as shown in Fig. 1.

- (1) Development of reentry flow.
  - (a) The flow behind it separates when the cavity stops growing. The liquid from this separation zone is drawn into the cavity by the prevailing pressure gradient and forms a reentry jet at the rear edge of the cavity.
  - (b) The reentry jet migrates upstream from the rear edge of the cavity to the front edge of the cavity.
- (2) Cavity shedding.
  - (c) At a certain point, the jet will intersect the cavity wall, break through the cavity wall, and flow downstream as a bubble vortex.

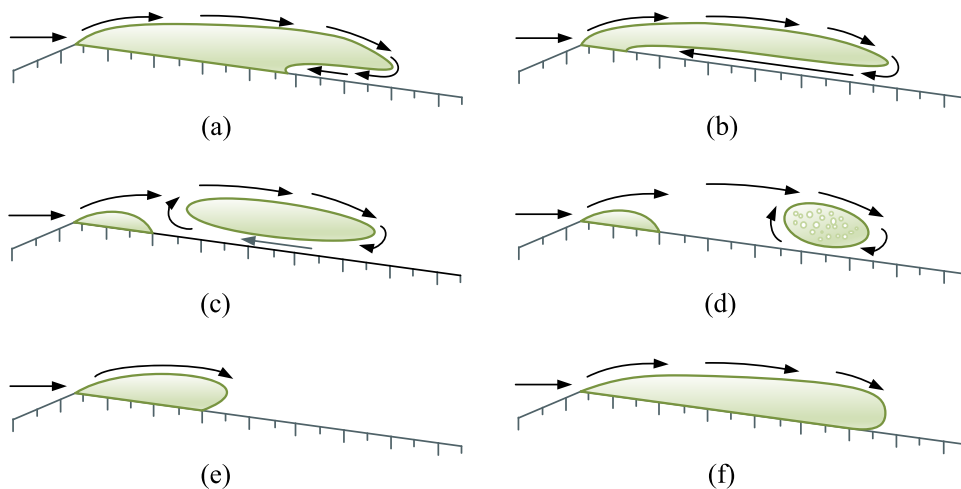


FIG. 1. Schematic illustration of cavity shedding caused by a reentry jet.<sup>25</sup> (a) and (b) Development of reentry flow, (c) and (d) cavity shedding, and (e) and (f) cavity growth. Light green represents the vaporous cavity, and the black arrows represent liquid streamlines.

- (d) The jet opposite to the flow direction brings considerable vorticity to the downstream foam, and the truncated cavity simultaneously regrows.
- (3) Cavity growth.
    - (e) The cavity grows steadily downstream with clear boundaries.
    - (f) The cavity reaches the maximum attached cavity length and enters the next period.

Considering the inaccuracy in URANS models for unsteady behaviors as a critical bottleneck in improving the prediction accuracy of numerical simulations for cavitating flow, the present study utilizes the renormalization group (RNG)  $k - \epsilon$  model with a modified turbulent eddy viscosity as the baseline URANS model and proposes a DD-URANS model to enhance the prediction performance of the aforementioned baseline model.

### A. Baseline URANS approach

In this study, the homogeneous equilibrium flow model is used for numerical computations; that is, the mixture of vapor and liquid phases is regarded as a homogeneous medium, and there is no relative velocity or pressure between the phases. Considering the transition rate between the phases, the baseline URANS equations in incompressible flows are obtained by taking the average values of the Navier–Stokes equations over time, which, in their form without body forces, are written as

$$\frac{\partial \rho_m}{\partial t} + \frac{\partial \rho_m \bar{u}_j}{\partial x_j} = 0, \tag{1}$$

$$\frac{\partial \rho_m \bar{u}_i}{\partial t} + \frac{\partial \rho_m \bar{u}_i \bar{u}_j}{\partial x_j} = -\frac{\partial \bar{p}}{\partial x_i} + \frac{\partial}{\partial x_j} \left[ \mu \left( 2S_{ij} - \frac{2}{3} \frac{\partial \bar{u}_k}{\partial x_k} \delta_{ij} \right) - \tau_{ij} \right], \tag{2}$$

where  $\bar{u}_i$  is the  $i$ th component of the mean velocity, that is,

$$\bar{u}_i(t) = \frac{1}{2T} \int_{t-T}^{t+T} u_i(t) dt, \tag{3}$$

in theory,  $T$  should be  $\ll$  resolved time scale.<sup>56</sup>  $\rho_m = \rho_l \alpha_l + \rho_v \alpha_v$  is the mixture density,  $\mu = \mu_l \alpha_l + \mu_v \alpha_v$  is the mixture dynamic viscosity,  $\rho_l$  is the liquid density,  $\rho_v$  is the vapor density,  $\alpha_l$  is the liquid fraction,

$\alpha_v$  is the vapor fraction,  $\mu_l$  is the liquid dynamic viscosity,  $\mu_v$  is the vapor dynamic viscosity,  $\bar{p}$  is the mean pressure, and  $\bar{S}_{ij} = 1/2(\partial\bar{u}_i/\partial x_j + \partial\bar{u}_j/\partial x_i)$  is the mean strain rate tensor. Compared with the form of the Navier–Stokes equation, there is an additional term  $\tau_{ij}$  in the URANS model, which is called the Reynolds stress and is written as

$$\tau_{ij} = \rho_m \overline{u'_i u'_j}. \quad (4)$$

The Reynolds stress tensor  $\tau_{ij}$  is a symmetric tensor that can be decomposed into an isotropic tensor  $\frac{2}{3}\rho_m k \delta_{ij}$  and an anisotropic tensor  $a_{ij}$

$$\tau_{ij} = \frac{2}{3}\rho_m k \delta_{ij} + a_{ij}, \quad (5)$$

where  $k$  is the turbulent kinetic energy and  $\delta_{ij}$  is the Kronecker delta. Therefore, it is essential to combine these equations with an appropriate turbulence model to form a complete model. The direct modeling of the Reynolds stress tensor is based on the Boussinesq hypothesis,<sup>57</sup> which in analogy with Newtonian flows assumes the Reynolds stress isotropic tensor to be a linear function of the mean velocity gradients such that

$$a_{ij}^L = -2\mu_t \left( \bar{S}_{ij} - \frac{1}{3} \frac{\partial \bar{u}_i}{\partial x_j} \delta_{ij} \right), \quad (6)$$

where  $\mu_t$  is the turbulent viscosity closed by the RNG  $k - \varepsilon$  model.

The mass fraction equation for vapor is as follows:

$$\frac{\partial \rho_v \alpha_v}{\partial t} + \frac{\partial \rho_v \alpha_v \bar{u}_i}{\partial x_i} = R^e - R^c, \quad (7)$$

where  $R^e$  is the evaporation rate, which indicates the mass of liquid that changes from liquid to vapor over a unit of time during the evaporation process, and  $R^c$  is the condensation rate, which can be simulated in the Zwart–Gerber–Belamri (ZGB) model established by Zwart *et al.*<sup>58</sup>

$$R^e = C_e \frac{3\alpha_{nuc}(1 - \alpha_v - \alpha_{ncg})\rho_v}{R_B} \sqrt{\frac{2 \max(p_{sat} - p, 0)}{3\rho_l}}, \quad (8)$$

$$R^c = C_c \frac{3\alpha_{nuc}\alpha_v\rho_v}{R_B} \sqrt{\frac{2 \max(p - p_{sat}, 0)}{3\rho_l}}, \quad (9)$$

where  $\alpha_{nuc}$  is the nucleation volume fraction,  $R_B$  is the bubble diameter,  $p_{sat}$  is the saturated vapor pressure,  $p$  is the local fluid pressure,  $C_e$  is the evaporation rate coefficient, and  $C_c$  is the condensation rate coefficient.

When phase transition phenomena occur, the divergence of the mean velocity  $\frac{\partial \bar{u}_i}{\partial x_i}$  is no longer equal to zero in the incompressible flow, which is denoted as  $S_p$  and is expressed as follows (more details of the numerical procedure for solving the mean velocity divergence are detailed in the Appendix):

$$S_p = \frac{\partial \bar{u}_i}{\partial x_i} = \left( \frac{1}{\rho_l} - \frac{1}{\rho_v} \right) (R^c - R^e). \quad (10)$$

Therefore, Eq. (6) is finally expressed as

$$a_{ij}^L = -2\mu_t \left( \bar{S}_{ij} - \frac{1}{3} S_p \delta_{ij} \right). \quad (11)$$

To calculate the turbulent viscosity  $\mu_t$ , the transport equations of the turbulent kinetic energy and dissipation rate are solved using the RNG  $k - \varepsilon$  model

$$\frac{\partial \rho_m k}{\partial t} + \frac{\partial \rho_m k \bar{u}_j}{\partial x_j} = \frac{\partial}{\partial x_j} \left[ \alpha_k (\mu_m + \mu_t) \frac{\partial k}{\partial x_j} \right] + \mathcal{P} - \rho_m \varepsilon, \quad (12)$$

$$\begin{aligned} \frac{\partial \rho_m \varepsilon}{\partial t} + \frac{\partial \rho_m \varepsilon \bar{u}_j}{\partial x_j} &= \frac{\partial}{\partial x_j} \left[ \alpha_\varepsilon (\mu_m + \mu_t) \frac{\partial \varepsilon}{\partial x_j} \right] \\ &+ C_{\varepsilon 1} \frac{\mathcal{P} \varepsilon}{k} - C_{\varepsilon 2} \rho_m \frac{\varepsilon^2}{k}, \end{aligned} \quad (13)$$

where  $\alpha_k$  and  $\alpha_\varepsilon$  are the reciprocals of the effective Prandtl numbers, and their empirical values are both 1.393. The model constants  $C_{\varepsilon 1}$  and  $C_{\varepsilon 2}$  are 1.42 and 1.68, respectively.  $\mathcal{P}$  is the generation term of the turbulent kinetic energy caused by the mean velocity gradient and is defined as follows:

$$\mathcal{P} = -\tau_{ij} \frac{\partial \bar{u}_i}{\partial x_j}. \quad (14)$$

For an ordinary case, the turbulent viscosity is calculated by  $\mu_t = \frac{C_\mu k^2 \rho_m}{\varepsilon}$ , which is overestimated in the mixed region. Therefore, a modified turbulent viscosity is defined, which significantly improves cloud-shedding simulations. The turbulent viscosity is previously modified<sup>27</sup> as follows:

$$\mu_t = f(\rho_m) \frac{C_\mu k^2 \rho_m}{\varepsilon}, \quad f(\rho_m) = \rho_v + \frac{(\rho_m - \rho_v)^n}{(\rho_l - \rho_v)^{n-1}}, \quad n = 10. \quad (15)$$

## B. Data-driven scheme

Higher-order eddy-viscosity models can be constructed for incompressible complex flows. The general expression of the higher-order eddy-viscosity model is determined as the sum of the linear and nonlinear components

$$\begin{aligned} a_{ij} &= \tau_{ij} - \frac{2}{3} \rho_m k \delta_{ij} = a_{ij}^L + a_{ij}^{NL} \\ &= -2\mu_t^L \left( \bar{S}_{ij} - \frac{1}{3} S_p \delta_{ij} \right) + a_{ij}^{NL} = -2\mu_t^L \frac{\varepsilon}{k} \hat{S}_{ij} + a_{ij}^{NL}, \end{aligned} \quad (16)$$

where

$$\hat{S}_{ij} = \frac{k}{\varepsilon} \left( \bar{S}_{ij} - \frac{1}{3} S_p \delta_{ij} \right) \quad (17)$$

is the dimensionless mean strain rate tensor and  $a_{ij}^{NL}$  represents the sum of the nonlinear terms. According to Zhang *et al.*,<sup>54</sup> the form of the nonlinear terms  $a_{ij}^{NL}$  can also be expressed in the generalized form of Pope<sup>59</sup>

$$\begin{aligned} a_{ij}^{NL} &= k \left( G^1 + 2\mu_t^L \frac{\varepsilon}{k^2} \right) \hat{S}_{ij} + kG^2 (\hat{S}_{ik} \hat{R}_{kj} - \hat{R}_{ik} \hat{S}_{kj}) \\ &+ kG^3 \left( \hat{S}_{ik} \hat{S}_{kj} - \frac{1}{3} \delta_{ij} \hat{S}_{mn} \hat{S}_{nm} \right) \\ &+ G^4 \left( \hat{R}_{ik} \hat{R}_{kj} - \frac{1}{3} \delta_{ij} \hat{R}_{mn} \hat{R}_{nm} \right) + \dots \end{aligned} \quad (18)$$

Let  $G^1 = G^1 + 2\mu_t^L \frac{\varepsilon}{k}$ ; Eq. (18) can then be expressed as

$$a_{ij}^{NL} = kG^1 \hat{S}_{ij} + kG^2 (\hat{S}_{ik} \hat{R}_{kj} - \hat{R}_{ik} \hat{S}_{kj}) + kG^3 \left( \hat{S}_{ik} \hat{S}_{kj} - \frac{1}{3} \delta_{ij} \hat{S}_{mn} \hat{S}_{nm} \right) + G^4 \left( \hat{R}_{ik} \hat{R}_{kj} - \frac{1}{3} \delta_{ij} \hat{R}_{mn} \hat{R}_{nm} \right) + \dots, \quad (19)$$

where  $G^n$  is a function of the invariants  $\lambda_i$ , defined as

$$\lambda_1 = \hat{S}_{mn} \hat{S}_{nm}, \quad \lambda_2 = \hat{R}_{mn} \hat{R}_{nm}, \quad \dots \quad (20)$$

The linear term is treated implicitly to enhance conditioning when solving the URANS equations. To compute  $\mu_t^L$ , the optimal eddy viscosity introduced by Wu, Xiao, and Paterson<sup>52</sup> is chosen as follows:

$$\mu_t^L = \arg \min_{\mu_t} \left\| a_{ij} - \left( -2\mu_t^L \frac{\varepsilon}{k} \hat{S}_{ij} \right) \right\|, \quad (21)$$

which minimizes the discrepancy between the anisotropy Reynolds stress tensor and its linear component.  $\| \cdot \|$  denotes the Frobenius norm of a matrix. The optimal eddy viscosity  $\mu_t^L$  can be computed by projecting the anisotropic stress tensor onto the strain rate tensor as follows:

$$\mu_t^L = -\frac{k}{\varepsilon} \frac{a_{ij} \hat{S}_{ij}}{\|\hat{S}_{ij}\| \|\hat{S}_{ij}\|}, \quad (22)$$

where  $a_{ij} \hat{S}_{ij}$  represents the double dot product of tensors.

In this study, data-driven techniques and high-fidelity data are used to construct the regression functions that predict the optimal eddy viscosity  $\mu_t^L$  and nonlinear part  $a_{ij}^{NL}$  of the anisotropic Reynolds stress tensor.

### 1. Parameter selection and regression function construction

From Eqs. (19) and (20), it can be seen that

$$a_{ij}^{NL} = f(\lambda_1, \lambda_2, \dots). \quad (23)$$

It can be found that there is a lack of information about cavitating flow in this hypothesis. First, the mixed-phase density  $\rho_m$  is an important physical quantity in cavitating flow because it determines the prediction accuracy of the turbulent viscosity component. Second, the URANS model has also been improved based on density in many modification methods. Similarly, the phase transition term  $S_p$  is crucial and determines the mass conservation equation of the vaporliquid flow. Therefore, the mixed-phase density term  $\rho_m$  and the phase transition term  $S_p$  are also included in the input, leading to the following functional mapping:

$$a_{ij}^{NL} = f(\lambda_1, \lambda_2, \dots, \hat{\rho}_m, \hat{S}_p), \quad (24)$$

where  $\hat{\rho}_m = \frac{\rho_m}{\rho_l}$ ,  $\hat{S}_p = \frac{S_p L}{u_\infty}$ ,  $L$  is the characteristic scale of the flow field, and  $u_\infty$  is the incoming flow velocity. To compute the optimal eddy viscosity, a mapping relationship is established as follows:

$$\mu_t^L = f_2(\lambda_1, \lambda_2, \dots, \hat{\rho}_m, \hat{S}_p), \quad (25)$$

### 2. Training strategy for multi-time data fusion

To improve the prediction accuracy of the baseline URANS model for unsteady cavitating flow, a multi-time data fusion method

for a temporal distribution is developed, as shown in Fig. 2. First, the flow field data are generated via the numerical simulation of a cavitating flow. Second, as shown in Fig. 2(b), the period of cavity shedding is calculated based on the fast Fourier transform (FFT) results obtained via the monitoring data. The flow field data in a single period can clearly represent the process of cavity development ( $t_1$  represents cavity initiation,  $t_2$  and  $t_3$  represent reentry flow growth, and  $t_4$  indicates that cavity shedding is completed). Therefore, to capture the unsteady characteristics of the flow field, the dataset needs to be composed of data of multiple time frames. Wróblewski *et al.*<sup>60</sup> selected the numerical simulation results of ten time frames in one period to describe the cavity shedding of the Clark-Y airfoil. Considering the dependence of data-driven technology on dataset,<sup>61,62</sup> the data from 20 time frames ( $t^1, t^2, t^3, \dots, t^{20}$ ) are selected between  $t_1$  and  $t_4$  for fusion to more fully capture the time evolution of the cavity. Finally, the corresponding neural networks are constructed for training based on the regression function relationship and the dataset established above.

As shown in Fig. 2(c), a combined neural network is employed to train the model. A fully connected neural network is composed of various neurons. The neurons are laid out in layers. The leftmost layer is called the input layer and is responsible for receiving input data. The rightmost layer is the output layer. We obtain neural network output data from this layer. The layers between the input and output layers are called hidden layers because they are invisible to the outside. There is no connection between neurons in the same layer. Each neuron in layer  $l$  is connected to all neurons in layer  $l-1$  (this is the meaning of the phrase fully connected), and the output  $c_j(l-1)$  of the neurons in layer  $l-1$  is the input of the neurons in layer  $l$ . Each connection between the two layers has a weight  $W$ , which is the model parameter that the neural network must learn. Considering the  $i$ th neuron node of the  $l$ th layer as an example, the value of this neuron is

$$z_i(l) = \sum_{j=1}^n W_{ij}(l) c_j(l-1) + b_i(l). \quad (26)$$

$z_i(l)$  is then applied to the activation function to obtain the final result  $c_i(l)$

$$c_i(l) = f[z_i(l)], \quad (27)$$

where  $b_i(l)$  are the bias and  $f$  is the activation function. The activation function in this network is a leaky rectified linear unit (leaky ReLU)<sup>63</sup> and is expressed as

$$f(x) = \begin{cases} \alpha x, & x < 0, \\ x, & x \geq 0, \end{cases} \quad (28)$$

where  $\alpha$  is taken as  $10^{-8}$ .

To minimize the error between the predicted and true values, gradient descent backpropagation is used to obtain the error of each layer, and the error of each layer is then used to update the weight of each layer to fit the model. The loss function is given by the root mean squared error (RMSE). The details of the optimized network architecture used in this study are listed in Table I.

### 3. Data-driven URANS model

In data-driven terminology, the flows used to construct the regression functions are the training flows, and the flow to be

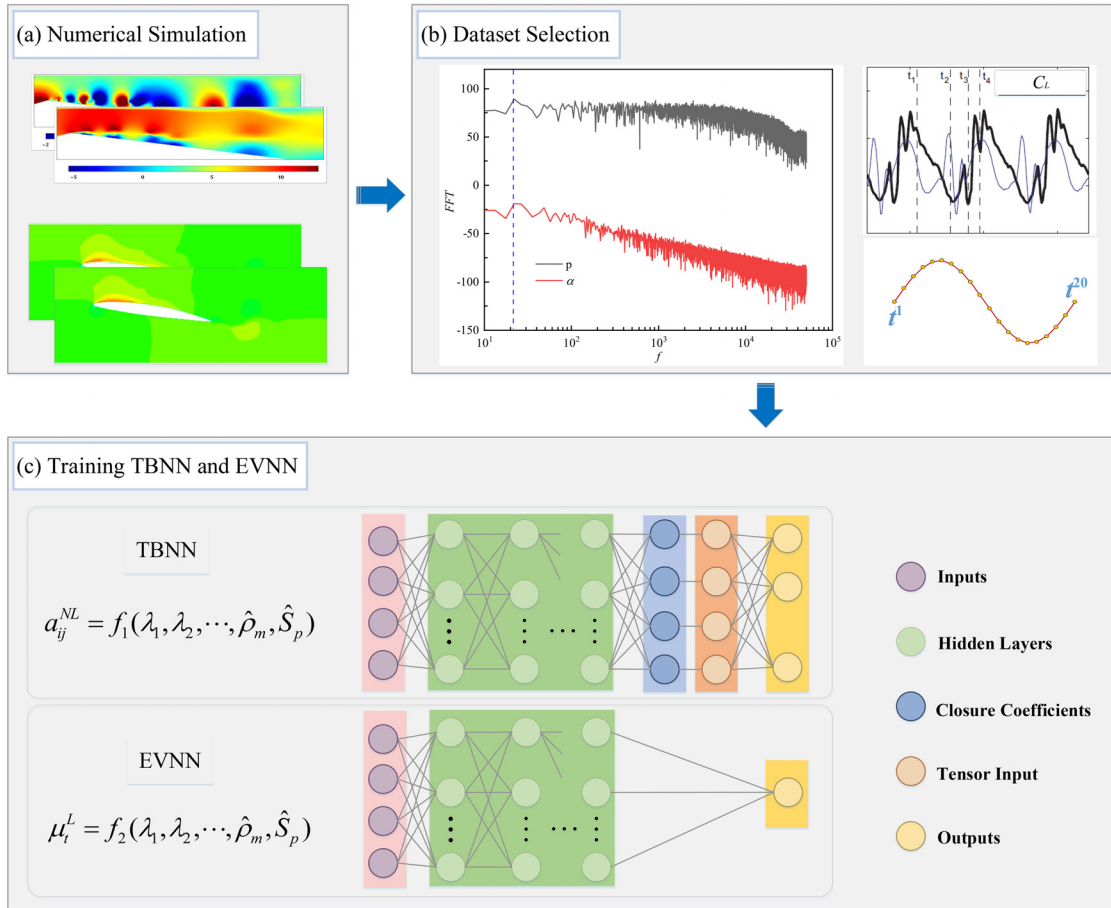


**FIG. 2.** Model training strategy. (a) Numerical simulation for flow field data. (b) Dataset selection. The graph containing red and black lines represents the FFT results of the flow field data. The graph with black and light blue lines represents the variation of the flow field data with time. The variation curve from  $t^1$  to  $t^{20}$  represents 20 time points within a single cycle of the flow field. (c) The upper image indicates tensor basis neural network (TBNN), and the lower image indicates the eddy viscosity neural network (EVNN).

predicted is the test flow. The procedure of the proposed DD-URANS model is illustrated in Fig. 3.

The LES approach is an effective and mainstream numerical simulation method for predicting cavitating flow that can accurately predict the unsteady characteristics of the flow.<sup>64</sup> Therefore, this study uses the LES approach to generate the target dataset and applies the modified RNG  $k - \varepsilon$  model mentioned above to obtain baseline dataset.

**TABLE I.** Neural network hyperparameters.

Parameters	TBNN	EVNN
Number of hidden layers	5	3
Number of nodes per layer	10	6
Activation function	Leaky ReLU	Leaky ReLU
Optimization	Adam	Adam
Regularization coefficient	0.005	0.005

A combined neural network is constructed as shown in Fig. 2(c), in which the output of neural network 1 [tensor basis neural network (TBNN)] is  $a_{ij}^{NL} = a_{ij}^{LES} - a_{ij}^{URANS}$ , and the output of neural network 2  $\mu_t^L$  [eddy viscosity neural network (EVNN)] is the eddy viscosity obtained via LES. The two artificial neural networks correspond to regression functions  $f_1$  and  $f_2$ , respectively.

After the simulation data are obtained, the 3D LES data are span-wise averaged and then linearly interpolated to correspond to the simulated 2D URANS data obtained under the coarse grid. The neural network is then trained based on the above dataset.

- (1) Perform baseline URANS operations on both the training and test flows to obtain the input features and  $a_{ij}^{URANS}$ .
- (2) Compute the discrepancy fields  $a_{ij}^{NL} = a_{ij}^{LES} - a_{ij}^{URANS}$  for the training flows and train the regression function  $f_1$  and  $f_2$ .

The obtained regression relationship is then used to modify and predict the cavitating flow. A detailed description of the DD-URANS model is provided in Algorithm 1.

ALGORITHM 1: Data-driven URANS method.

**Input:** Computational domain  $\Omega \in (x, y)$ , number of meshes  $N$ , point coordinates  $[(x_1, y_1), (x_2, y_2), \dots, (x_k, y_k), \dots, (x_N, y_N)]$  ( $k \in [1, N]$ ), initial conditions, boundary conditions, turbulence model, cavitation model, and iteration steps  $T_n$  for baseline URANS model.

**Output:** Instantaneous and mean flow field results.

```

1 for step = 1 to  $T_n$  do
2   for  $k = 1$  to  $N$  do
3     Perform baseline URANS on the test flow to obtain the
       input features  $\lambda_1, \lambda_2, \hat{\rho}_m, \hat{S}_p$ , and  $a_{ij}^{URANS}$  of point  $(x_k, y_k)$ 
       [see 3(a)];
4     Apply the trained regression function  $f_1$  to predict the non-
       linear terms  $a_{ij}^{NL}$  of point  $(x_k, y_k)$  [see 3(b)];
5     Apply the trained regression function  $f_2$  to predict the opti-
       mal eddy viscosity  $\mu_t^L$  of point  $(x_k, y_k)$  [see 3(b)];
6     Substitute the predicted  $a_{ij}^{NL}$  and  $\mu_t^L$  values in the URANS
       equations for the anisotropy stress tensor  $a_{ij}$  of point  $(x_k,$ 
        $y_k)$ , as shown in Eq. (16);
7     Solve the developed DD-URANS model to update the
       velocity field and pressure field by PISO algorithm;
8   end
9   Predict the flow fields and output the instantaneous flow and
       mean flow field results [see 3(c)].
10 end
    
```

C. High-fidelity data for the data-driven model

1. High-fidelity LES numerical simulations

The LES approach is used in this study to obtain the required high-fidelity data. The LES equations are spatially Favre-filtered as follows:

$$\frac{\partial \rho_m}{\partial t} + \frac{\partial \rho_m \tilde{u}_j}{\partial x_j} = 0, \tag{29}$$

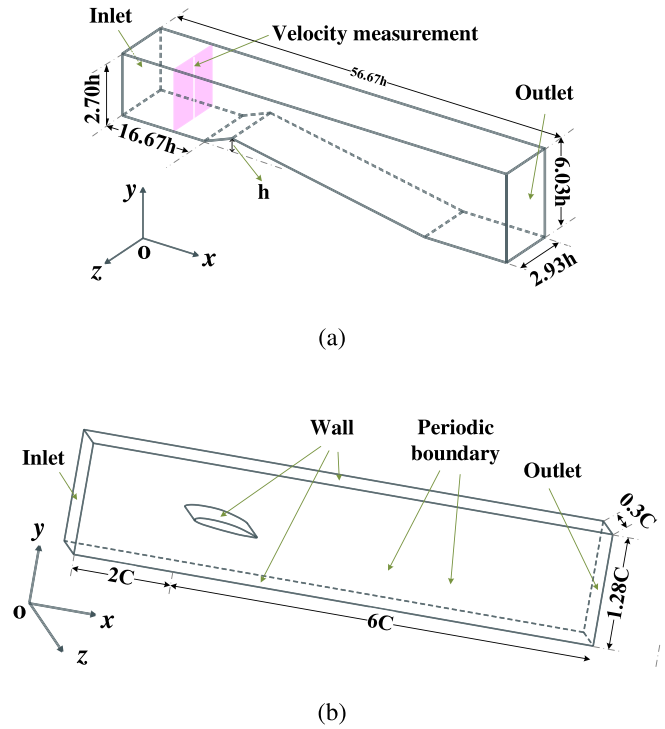


FIG. 4. Computational domain of a (a) Venturi-type convergent-divergent nozzle and (b) NACA66 hydrofoil.

$$\frac{\partial \rho_m \tilde{u}_i}{\partial t} + \frac{\partial \rho_m \tilde{u}_i \tilde{u}_j}{\partial x_j} = -\frac{\partial \tilde{p}}{\partial x_i} + \frac{\partial}{\partial x_j} \left[ \mu \left( 2\tilde{S}_{ij} - \frac{2}{3} \frac{\partial \tilde{u}_k}{\partial x_k} \delta_{ij} \right) - \tau_{ij} \right], \tag{30}$$

where  $\tilde{u}_i$  is the filtered  $i$ th velocity component,  $\tilde{p}$  is the filtered pressure,  $\tilde{S}_{ij} = 1/2(\partial \tilde{u}_i/\partial x_j + \partial \tilde{u}_j/\partial x_i)$  is the filtered strain-rate tensor, and  $\tau_{ij} = \rho_m(\tilde{u}_i \tilde{u}_j - \tilde{u}_i \tilde{u}_j)$  are the SGS stress, which are modeled using the wall-adapting local-eddy viscosity (WALE) model.<sup>55</sup>

08 April 2024 03:25:06

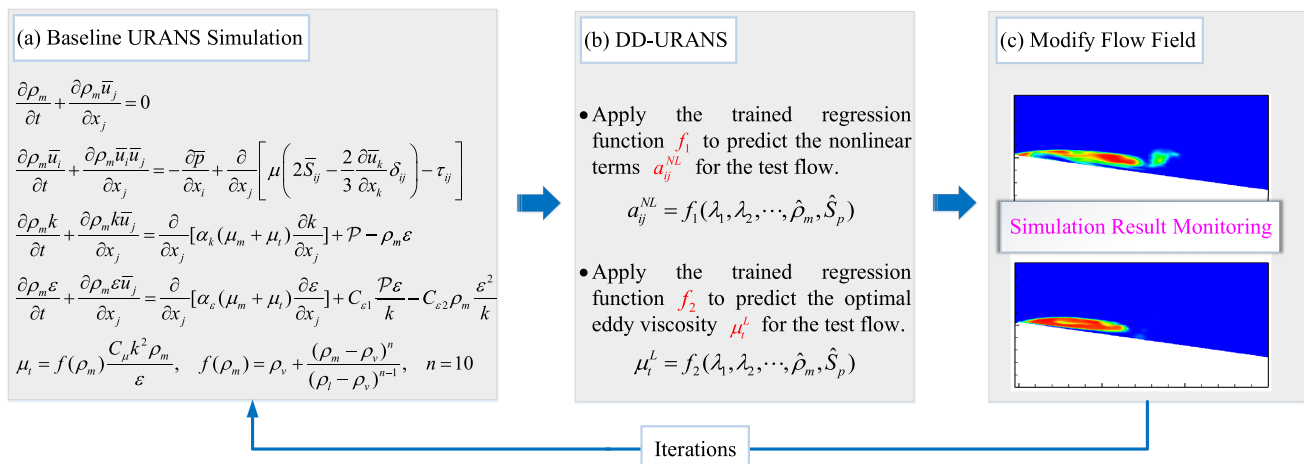


FIG. 3. Data-driven framework. (a) Governing equations and transport equations for baseline URANS simulations. (b) DD-URANS model. The trained regression functions  $f_1$  and  $f_2$  are applied to modify the baseline URANS equations. (c) Monitor the simulation results predicted by the DD-URANS model.



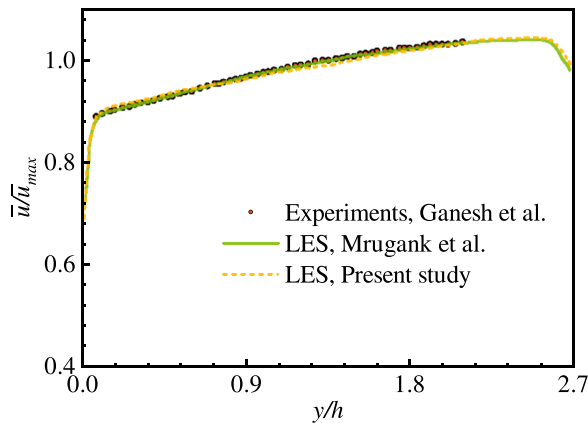


FIG. 5. Comparison of the inflow velocity profile at the velocity measurement plane with the experiment data from Ganesh, Makiharju, and Ceccio<sup>65</sup> and LES data from Bhatt and Mahesh.<sup>66</sup>

2. Case setup

In this study, a Venturi tube with a shrink-diverging nozzle and a NACA66 hydrofoil are selected as the basic cases. These two cases exhibit a typical separation flow and cavity shedding mechanism, and the related experimental verification results are obtained in greater detail. The saturated vapor pressure used is set according to the water temperature (24°).

Figure 4(a) illustrates the geometry of a convergent-divergent nozzle of the Venturi type adopted in the simulations. A sharp ridge is formed in the throat, causing a greater pressure drop, and the height of the throat is  $h$ . The surface indicated by the green arrow represents the fluid inlet and outlet. The mean fluid flows from the inlet to the outlet in the  $x$  direction, extending  $56.67h$  downstream. The length and width of inlet are  $2.93h$  and  $2.70h$ , respectively, and the length and width of outlet are  $2.93h$  and  $6.03h$ , respectively. The angle of the converging component is  $11.3^\circ$ , and the angle of the diverging section is

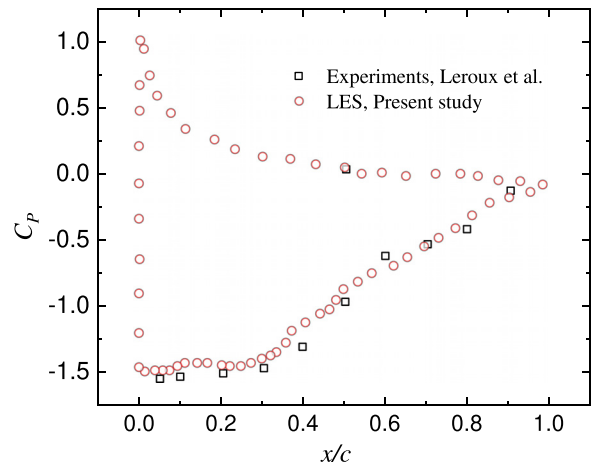


FIG. 6. Comparison of the mean pressure distribution around the NACA66 hydrofoil.

TABLE II. Datasets used for model training and testing.

Training cases	Testing case
Venturi $\sigma = 2.0, 2.2, 2.7$ ; NACA66 $\sigma = 0.8, 1.5$	Venturi $\sigma = 2.5$

$7.1^\circ$ . The inlet velocity is set to  $u_l = 7.4$  m/s, and at the outlet boundary, the outlet pressure changes with the cavitation number. The cavitation number is defined as  $\sigma = (p_\infty - p_v) / (0.5\rho_l u_\infty^2)$ , where  $p_\infty$  is the environmental pressure varying with cavitation number,  $p_v$  is the saturated vapor pressure,  $\rho_l = 998.2$  kg/m<sup>3</sup> is the liquid water density, and the other boundary conditions are set to no slip. The flow is simulated at a Reynolds number of  $Re = 118\,000$ .

The computational domain of the NACA66 hydrofoil is illustrated in Fig. 4(b). The hydrofoil chord length is  $C = 0.15$  m, and the

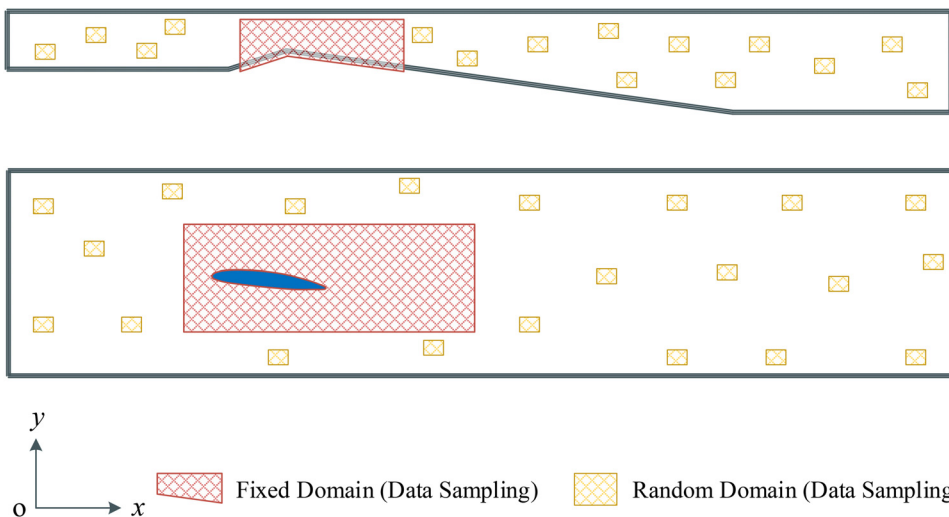


FIG. 7. Data sampling distribution.

TABLE III. Datasets used for generalizability of predictions.

Training cases	Testing case
Venturi $\sigma = 2.0, 2.2, 2.7$ ; NACA66 $\sigma = 0.8, 1.5$	Clark-Y hydrofoil $\sigma = 0.8$

foil is fixed within a 1.2-m-long and 0.192-m-wide square test section. The attack angle is  $6^\circ$ . The inflow velocity is  $u_i = 5.0$  m/s,  $Re = 750\,000$ , and the static pressure is adjusted to vary the cavitation number.

### 3. Validation of high-fidelity LES simulation results

For the Venturi flow ( $\sigma = 2.5$ ), the velocity profile along the normal direction of the wall is compared with the experiment data from Ganesh, Makiharju, and Ceccio<sup>65</sup> and LES data from Bhatt and Mahesh<sup>66</sup> at the mid-line of the plane indicated in Fig. 4(a), and a

comparison of these results is shown in Fig. 5. It is found that the LES approach used in this study can obtain a more accurate cavity structure. For NACA66, the mean pressure distribution around the hydrofoil ( $\sigma = 1.5$ ) is in good agreement with the experiment data from Leroux, Astolfi, and Billard,<sup>67</sup> as shown in Fig. 6. Therefore, other cases with different cavitation numbers can be computed based on this LES approach to obtain high-fidelity data and realize the modification of the baseline URANS model.

### III. RESULTS AND DISCUSSION

The cases used for the model training and testing are listed in Table II. The cases with cavitation numbers of 2.0, 2.2, and 2.7 for a Venturi flow and two cases with cavitation numbers of 0.8 and 1.5 for a NACA66 hydrofoil are used to train the neural network, and the case with a cavitation number of 2.5 for a Venturi flow is used for testing. However, the multi-time flow field characteristics obtained under various cases are selected to train the neural network, which resulted in an abnormally large amount of data. Therefore, this study performs

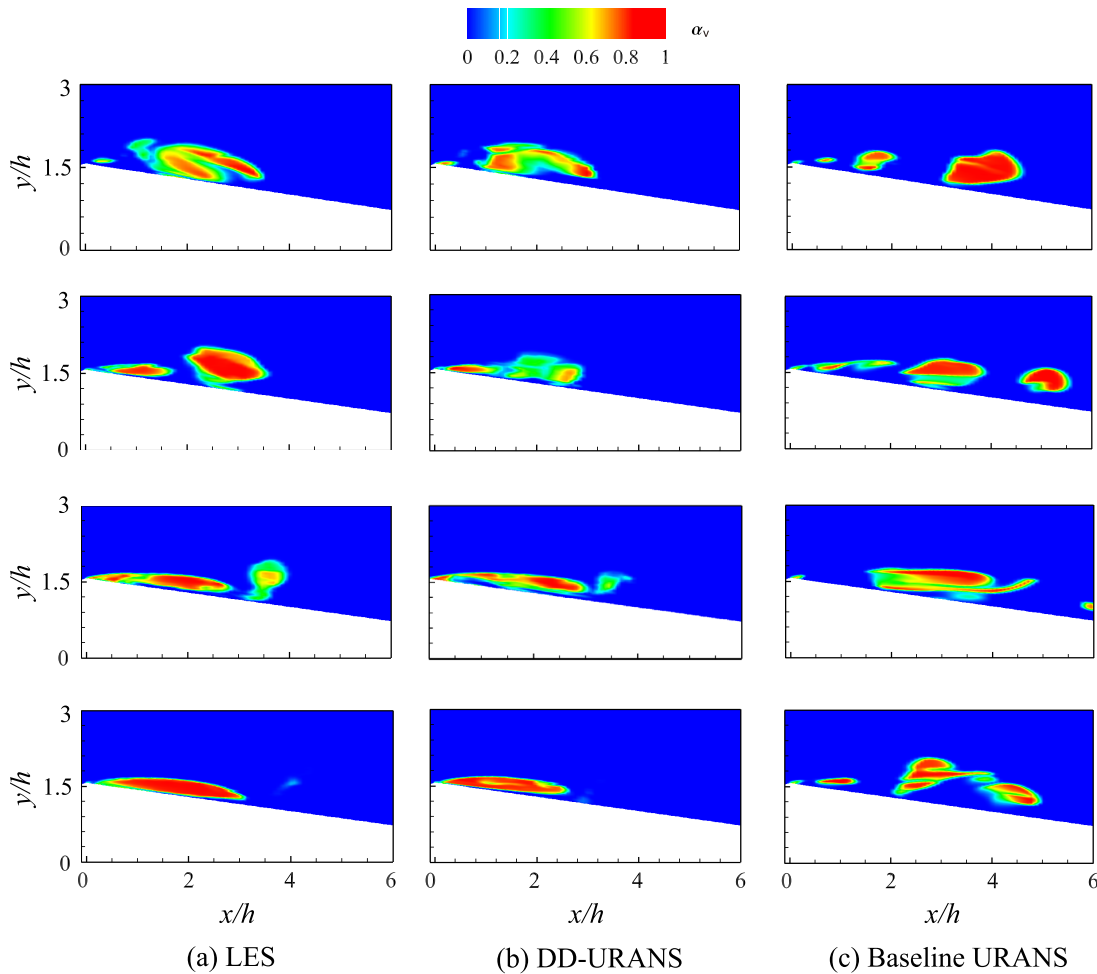


FIG. 8. Contours of the instantaneous periodic shedding obtained via the (a) LES, (b) DD-URANS, and (c) baseline URANS models. The first row shows that cavity begins to grow, the second and third rows show the development of cavity, and the fourth row shows the maximum length of cavity.

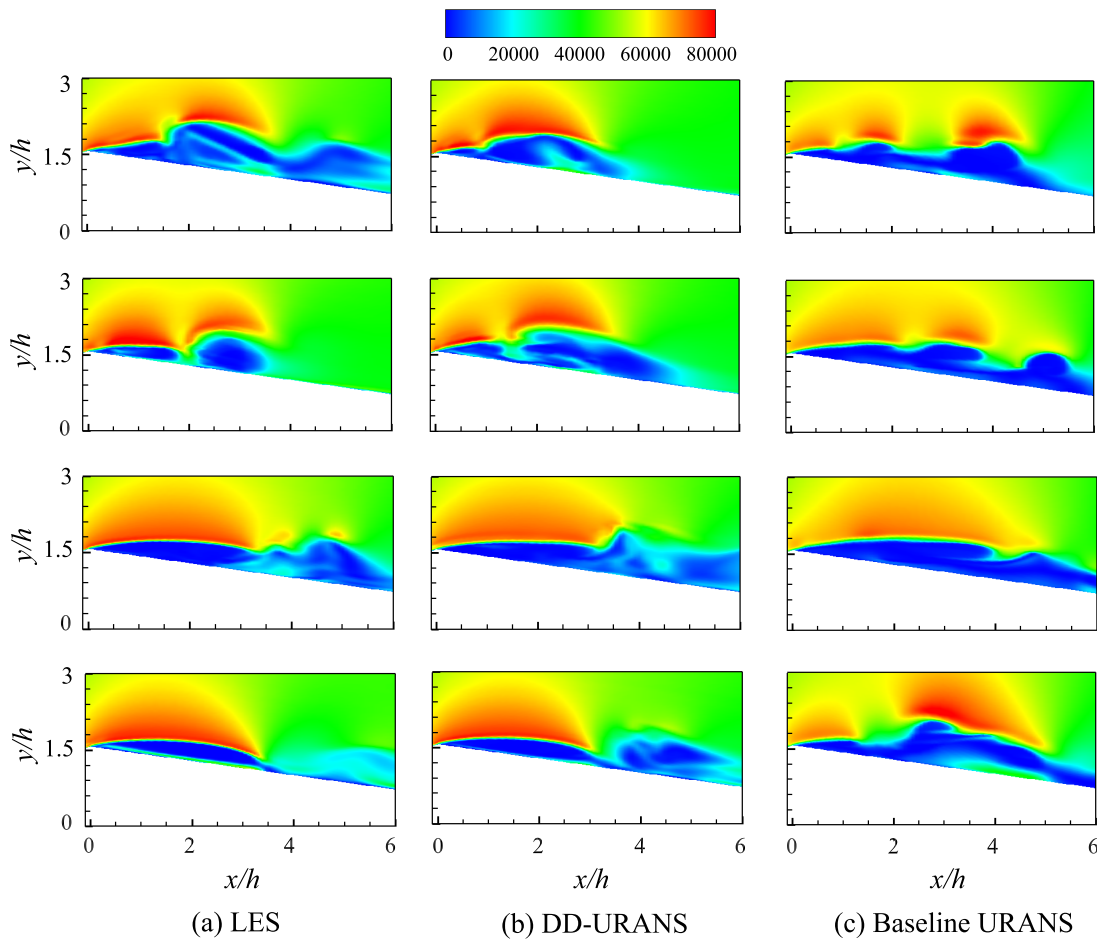


FIG. 9. Contours of the instantaneous pressure obtained via the (a) LES, (b) DD-URANS, and (c) baseline URANS models.

fixed and random sampling for the flow at the selected time, as shown in Fig. 7. The fixed domain is shown in red in Fig. 7, and the remainder of the domain can be used for random sampling. The random sampling data comprised 20% of the full flow field data.

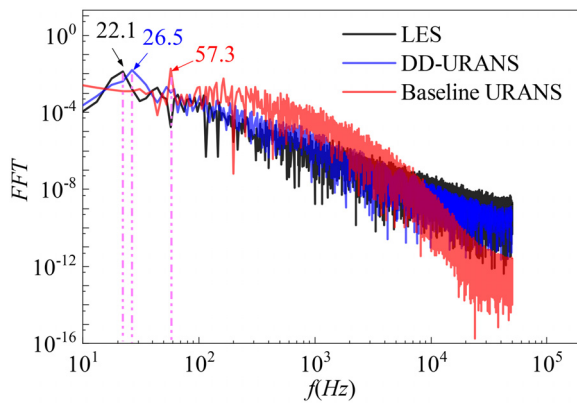


FIG. 10. Corresponding FFT results for the instantaneous volume fraction of vapor.

The prediction advantages of the DD-URANS model will next be analyzed and discussed in terms of the following three aspects. First, the performance of the DD-URANS model is analyzed to predict instantaneous periodic shedding. Subsequently, the mean flow fields are discussed. Finally, the generalizability of the DD-URANS model is further verified by testing using a Clark-Y airfoil (see Table III for the datasets).

### A. Venturi flow—instantaneous periodic shedding

The baseline URANS results are those obtained using the modified RNG simulations. The data-driven results are denoted as DD-URANS in the figure legends. The instantaneous periodic shedding of the divergent section of the Venturi flow computed via the LES, DD-URANS, and baseline URANS models is shown in Fig. 8. It can be seen that the cavitation inside of the flow vortices is captured by the LES simulation results. Figure 8(a) shows that the cavity gradually grows from the apex of the wedge and flows downstream along with the detached cloud from the previous cavity as it travels upward. The cavity then reaches its maximum length and exhibits a stable cavity interface. When the cavity is further generated, the vapor cloud begins to collapse and the next cavity begins to grow. Figure 8(c) shows the

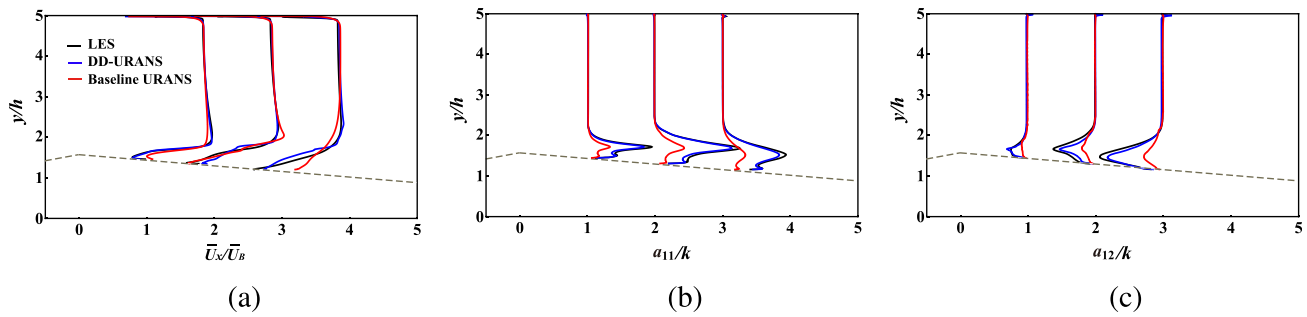


FIG. 11. Profiles simulated by LES, DD-URANS, and baseline URANS models. (a) Mean streamline velocity  $\bar{U}_x/\bar{U}_B$ , (b) normal stress component  $a_{11}/k$ , and (c) shear stress component  $a_{12}/k$ .

computational results for the baseline URANS model. It can be observed that the cavity gradually grows from the apex of the wedge, the maximum length of the cavity is significantly shorter than the results of the LES simulation, and no obvious periodic vapor shedding is captured. In the prediction results of the DD-URANS model [see Fig. 8(b)], it is found that the cavity experienced three stages: initial growth, achievement of maximum length, and shedding. The cavity shedding period is approximately the same as that in the LES simulation results.

Accordingly, the time evolution of the pressure distribution predicted by LES, DD-URANS, and baseline URANS models is shown in Fig. 9. From the LES results [Fig. 9(a)], it can still be seen that the cavity gradually grows to the maximum length. The prediction results of DD-URANS model are closer to the LES results than the original URANS results in capturing the time evolution of cavity, which further verifies the prediction advantages of the DD-URANS model.

In the numerical computation process, a monitoring surface is set up in the cavitation area to monitor the instantaneous vapor volume fraction, and FFT is performed based on the monitored signal. As shown in Fig. 10, the FFT obtained using the LES approach exhibits a peak value at  $f = 22.1$ . The corresponding peak values of the DD-URANS and baseline URANS models are 26.5 and 57.3, respectively, which further confirms that the URANS model has limited predictive abilities for instantaneous cavity shedding, and also verifies the improved predictive performance of the DD-URANS model.

### B. Venturi flow—mean flow field

This section describes the prediction performance of the DD-URANS model for the mean flow field in the cloud cavitation regime. Figure 11(a) presents the mean streamline velocity computed by the LES, DD-URANS, and baseline URANS models. As shown in Fig. 11(a), the baseline URANS model overestimates the cavity length, whereas the DD-URANS model is better at simulating the vapor regions. The corresponding profiles for the anisotropic Reynolds stress are shown in Figs. 11(b) and 11(c), respectively, which further verifies that the DD-URANS model is superior to the URANS model.

The contour of the mean vapor volume fraction simulated by the DD-URANS model is compared with the LES and baseline URANS results in Fig. 12. The LES results show an obvious closed-loop reentry jet phenomenon, which is conducive to cavity shedding and is quite different from the simulation results of URANS. Compared with the baseline URANS model, the DD-URANS model captures the thickness and length of the cavity more accurately.

To compare the results more clearly, Fig. 13 plots the profiles of the mean vapor volume fraction extracted at different axis positions ( $x/h = 0.5, 1, 2, 3, 4$ ) along the  $y$  axis on the surface of the divergent section. It can be seen from the profiles that the DD-URANS model predicts the cavity volume more accurately than the other models. When  $x = 4h$ , the cavity predicted by the LES approach has exhibited shedding ( $\langle \alpha_v \rangle = 0.0$ ), and the simulation results of the baseline URANS model show that the mean vapor volume fraction is still not

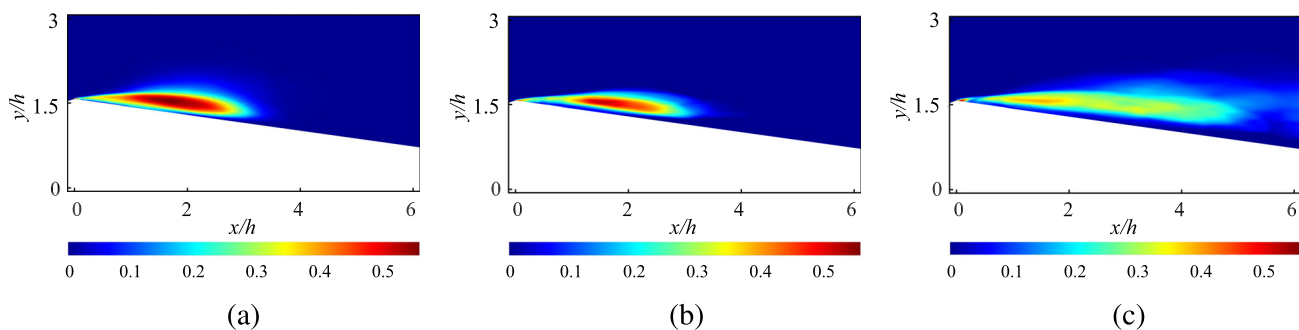


FIG. 12. Contours of the mean vapor volume fraction  $\langle \alpha_v \rangle$  from the (a) LES, (b) DD-URANS, and (c) baseline URANS models.

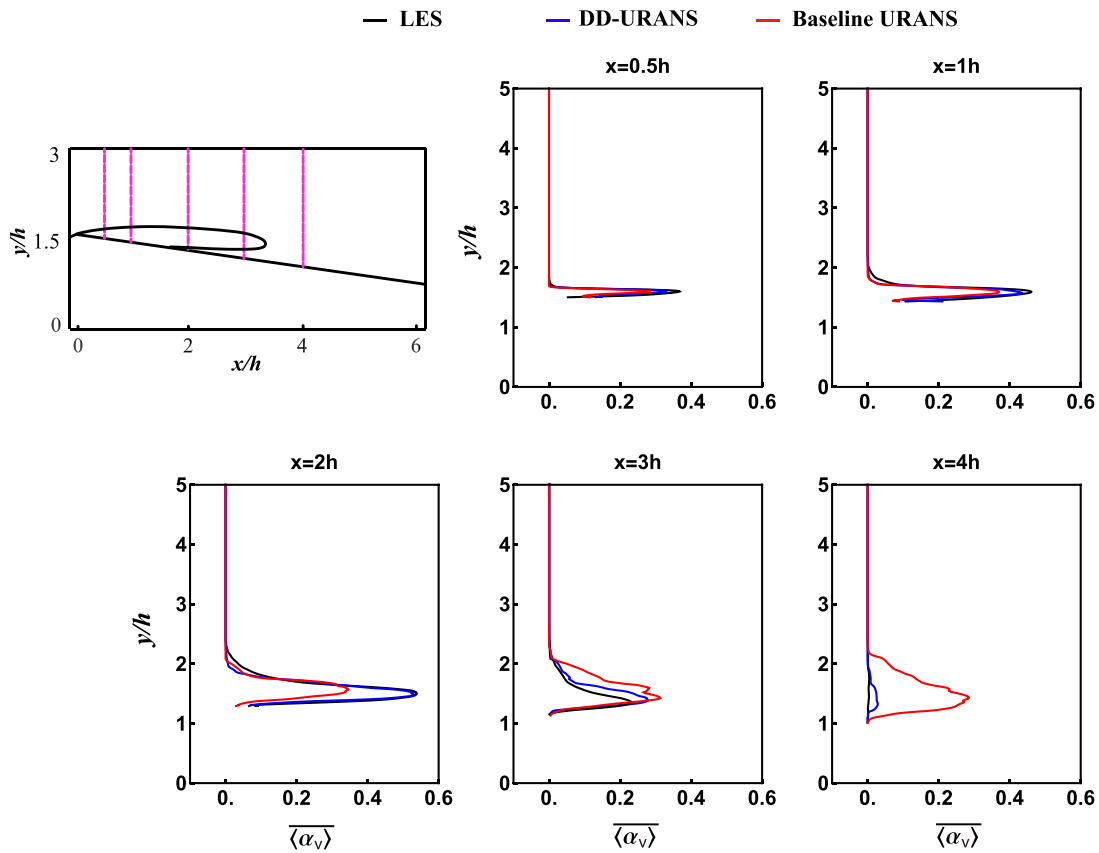


FIG. 13. Profiles of the mean vapor volume fraction simulated by the LES, DD-URANS, and baseline URANS models at five locations ( $x/h = 0.5, 1, 2, 3, 4$ ).

zero. However, compared with the baseline URANS model, the DD-URANS model significantly improves the prediction accuracy.

Compared with the baseline URANS model, the DD-URANS model can more accurately predict the cavity shedding and pressure evolution of cloud cavitation. Therefore, the DD-URANS model is further used to predict the development of small and medium-sized cavity

and obtain the mean vapor volume fraction results as shown in Figs. 14 and 15, respectively. The results show that DD-URANS model is superior to the baseline URANS model. However, the DD-URANS model cannot predict the evolution of cavitation inception well, because the relevant low-pressure structures responsible for cavitation inception are very small, which lead to inability of predicting the pressure histories

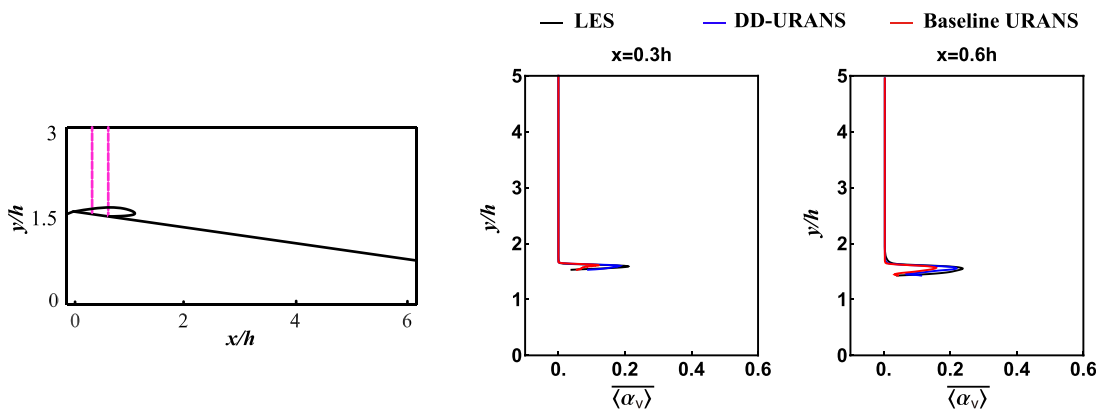


FIG. 14. Small-sized cavity: profiles of the mean vapor volume fraction simulated by the LES, DD-URANS, and baseline URANS models at two locations ( $x/h = 0.3, 0.6$ ).

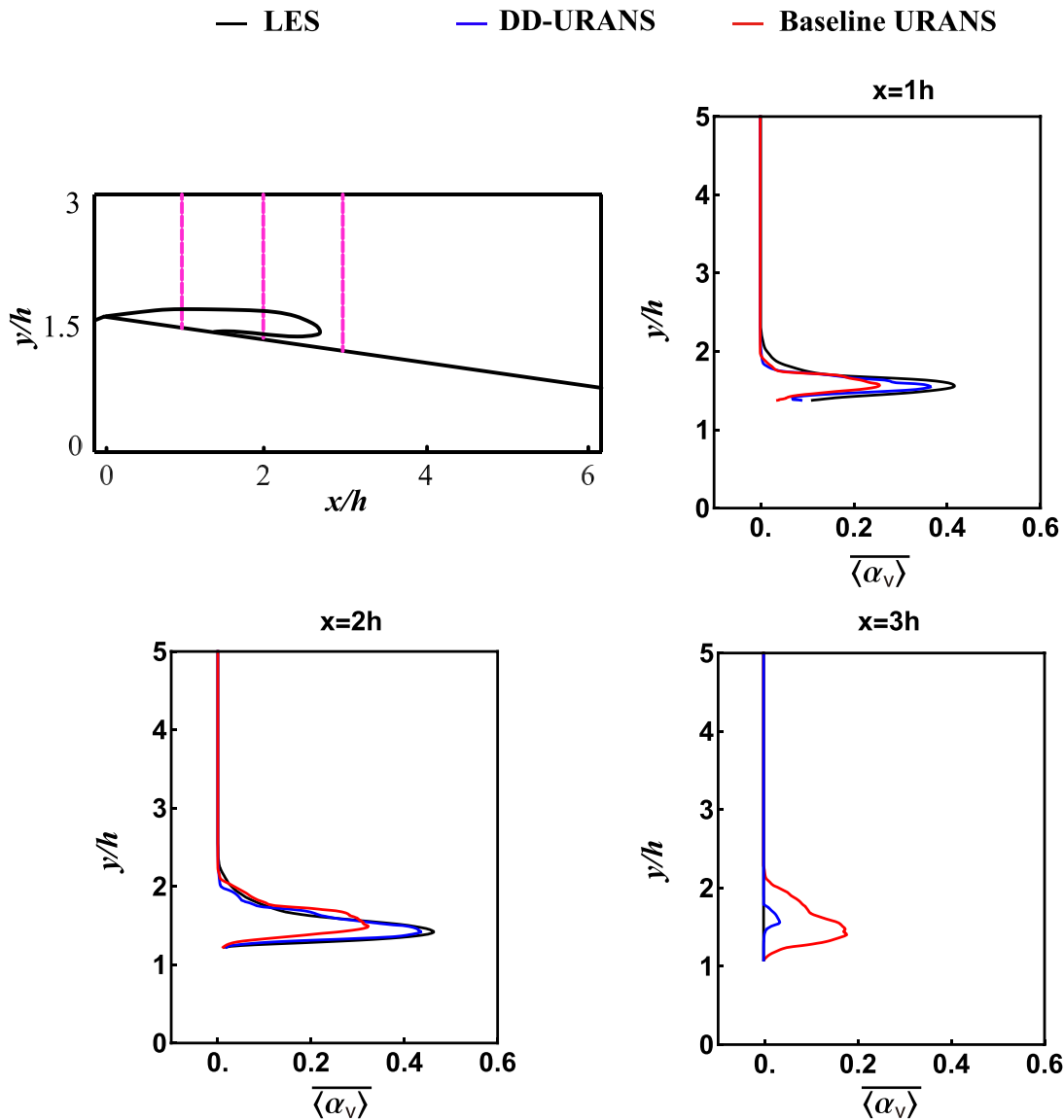


FIG. 15. Medium-sized cavity: profiles of the mean vapor volume fraction simulated by the LES, DD-URANS, and baseline URANS models at three locations ( $x/h = 1, 2, 3$ ).

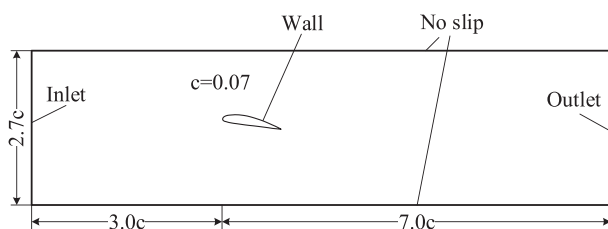
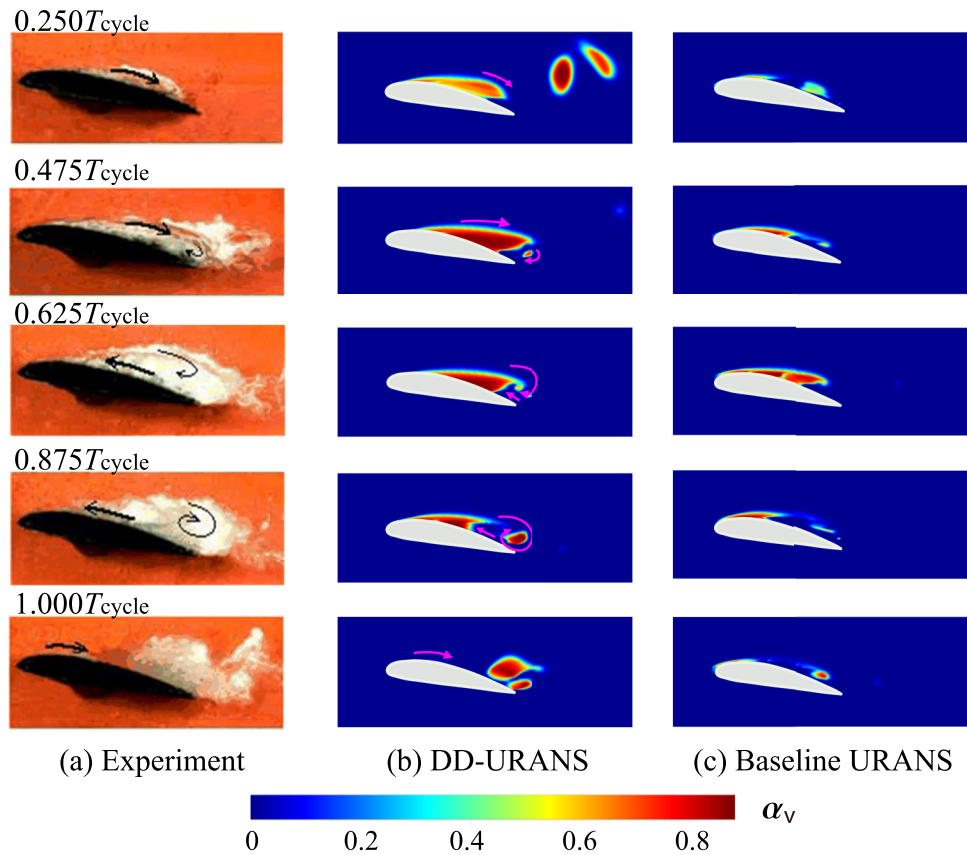


FIG. 16. Computational domain and boundary conditions.

experienced by nuclei in the uid.<sup>4</sup> This may need extra algorithms for in-depth research, and this will be an interesting topic in future work.

### C. Clark-Y hydrofoil—generalizability of predictions

To further explore the predictive performance of the DD-URANS model, the previously trained model is directly applied to Clark-Y hydrofoil flows. The computational domain is considered with the boundary conditions shown in Fig. 16. The chord length is  $c = 0.07$  m, and the attack angle is  $8^\circ$ . The Clark-Y hydrofoil is located in a channel with a length of  $10c$  and a height of  $2.7c$ .



**FIG. 17.** Clark-Y hydrofoil: contours of the instantaneous periodic shedding obtained via the (a) experimental results of Huang *et al.*,<sup>68</sup> (b) DD-URANS model, and (c) baseline URANS model.

Considering the boundary conditions, the wall is set at the hydrofoil surface, and nonslip is imposed at the top and bottom boundaries of the channel. The velocity at the inlet is  $u_\infty = 10 \text{ m/s}$  with a corresponding Reynolds number of  $Re = 700\,000$ . The outlet pressure is adjusted according to the cavitation number  $\sigma = 0.8$ . The Clark-Y hydrofoil is simulated using the baseline URANS and DD-URANS models, and the results are compared with the experimental results of Huang *et al.*<sup>68</sup> The contours of the instantaneous periodic shedding are presented in Fig. 17. As observed in the experiments, Fig. 17(a) shows that a cavity appears in the vicinity of the leading edge, grows to the maximum length, subsequently is shed, and finally collapses downstream. This instantaneous periodic shedding is not captured by the baseline URANS model [see Fig. 17(c)], while it is captured by the DD-URANS model [see Fig. 17(b)]. The time evolution of pressure distribution obtained from DD-URANS and URANS models is shown in Fig. 18. The time evolution of pressure is consistent with the instantaneous periodic shedding of cavity.

Table IV lists the cavity frequency obtained via the experimental data from Huang *et al.*,<sup>68</sup> modified partially averaged Navier–Stokes (PANS),  $f_k = 0.8$  PANS,  $f_k = 0.5$  PANS, baseline URANS model, and DD-URANS model, where  $f_k$  represents the unresolved-to-total ratios of the kinetic energy. The shedding frequency predicted by the DD-URANS model is 26.2, and the error obtained with the experimental

results is 8.62%, which is lower than the prediction results obtained via the other four models and demonstrates the advantages of the DD-URANS model for predicting unsteady cavitating flows.

Figure 19 shows the mean velocity profiles obtained at three locations ( $x/c = 0.2, 0.4, 0.6$ ) using the experimental results of Wang, Senocak, and Wei,<sup>69</sup> DD-URANS model, and baseline URANS model. It can be seen that the DD-URANS model yields a better agreement with the experimental results, whereas the baseline URANS model overestimates the length of the cavity.

#### IV. CONCLUSIONS

An implicit data-driven URANS framework is proposed to analyze the unsteady characteristics of cavitating flow. In this framework, the velocity divergence is obtained with the rate of the cavitation-induced phase transition and is used to calculate the anisotropic Reynolds stress through a high-order turbulence viscosity model. The linear and nonlinear parts of the anisotropic Reynolds stress tensor in this model are trained and predicted using implicit and explicit methods via two neural networks to overcome the ill-conditioning of the URANS equations and improve the computational stability, respectively. The machine learning model is trained using the numerical results obtained via LES. The training cases consisted of flows in a Venturi tube at cavitation numbers of 2.0, 2.2, and 2.7, as well as flows around a NACA66 hydrofoil at a

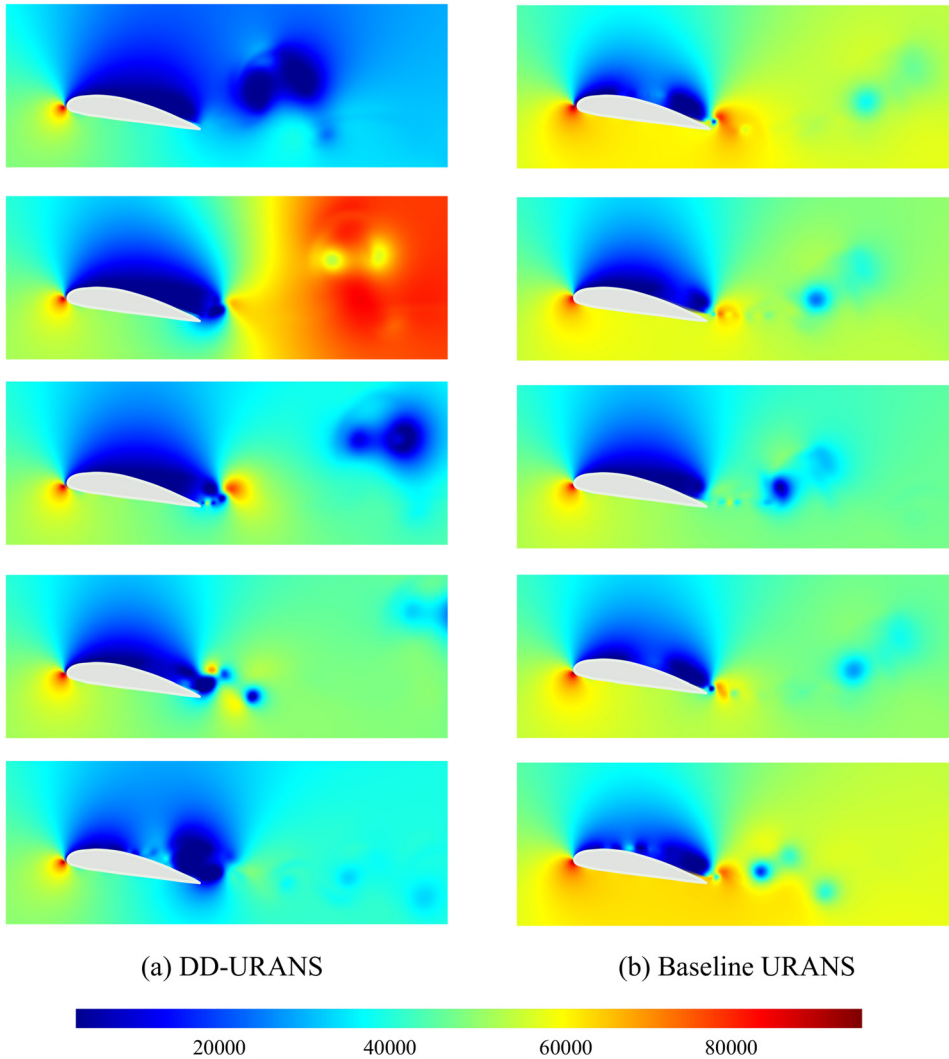


FIG. 18. Clark-Y hydrofoil: contours of the instantaneous pressure obtained via the (a) DD-URANS model, and (b) baseline URANS model.

cavitation number of 0.8. Furthermore, to improve the ability of this model to calculate the unsteady characteristics of cavitating flow, a multi-time data fusion method in a temporal distribution is developed to construct a training dataset.

TABLE IV. Comparisons of the flow quantities obtained via different approaches.

Case	Frequency (Hz)	Error
Experiment Huang <i>et al.</i> <sup>68</sup>	24.1	...
Modified PANS	30.9	28.22%
$f_k = 0.8$ PANS	27.7	14.94%
$f_k = 0.5$ PANS	41.5	72.20%
Baseline URANS	27.8	15.45%
DD-URANS	26.2	8.62%

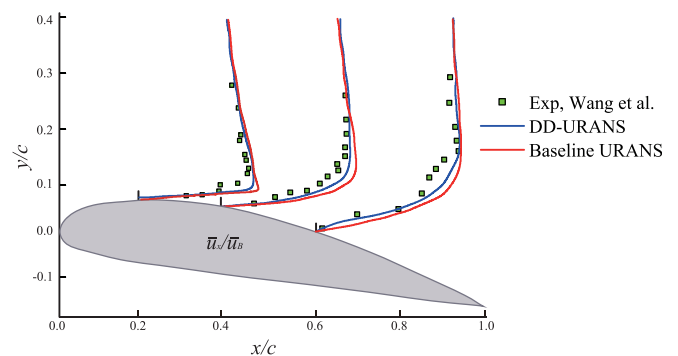


FIG. 19. Clark-Y hydrofoil: profiles of the mean velocity obtained via the experimental results of Wang, Senocak, and Wei,<sup>69</sup> DD-URANS model, and baseline URANS model at three locations ( $x/c = 0.2, 0.4, 0.6$ ).



Two cases are used to evaluate the computational accuracy of the DD-URANS model. We analyzed the unsteady development of the cavity, mean velocity, and vapor volume fraction for the flow in the Venturi tube at a cavitation number of 2.5. The results obtained with the DD-URANS model are in better agreement with those of the LES compared with the baseline URANS results. For the flow around a Clark-Y hydrofoil at a cavitation number of 0.8, the predicted results are compared with the baseline URANS and experimental results. The unsteady flow characteristics, such as the appearance, growth, shedding off, and collapse downstream of the cavity, are accurately obtained using the DD-URANS model. The error in the shedding frequency of the cavity predicted by the DD-URANS model is 8.62%, which is lower than the error of the URANS model relative to the experiment (15.45%). In addition, the Reynolds numbers of the Venturi tube and Clark-Y hydrofoil during the testing flow conditions are 118 000 and 70 000, respectively, which also shows that the DD-URANS model has the generalization ability on the Reynolds number distribution.

Overall, the computational accuracy of the DD-URANS model is much higher than that of the baseline URANS model that is commonly used for cavitating flow. Furthermore, it is shown that the developed model exhibits an excellent generalization ability for predicting both inner and outer flows, as well as flows around objects of different shapes. The DD-URANS model provides a novel approach for simulating complex unsteady multiphase flows in engineering applications.

**ACKNOWLEDGMENTS**

This work was supported by the National Natural Science Foundation of China (Nos. 12202291, 12122214, 12272382, 12293000, 12293003, and 12293004) and the Youth Innovation Promotion Association CAS (No. 2022019).

**AUTHOR DECLARATIONS**

**Conflict of Interest**

The authors have no conflicts to disclose.

**Author Contributions**

**Zhen Zhang:** Conceptualization (equal); Methodology (equal); Writing – original draft (equal). **Jingzhu Wang:** Formal analysis (equal); Writing – review & editing (equal). **Renfang Huang:** Data curation (supporting); Writing – review & editing (supporting). **Rundi Qiu:** Data curation (supporting); Investigation (supporting). **Xuesen Chu:** Validation (supporting). **Shuran Ye:** Validation (supporting). **Yiwei Wang:** Methodology (equal); Supervision (equal). **Qingkuan Liu:** Writing – review & editing (supporting).

**DATA AVAILABILITY**

The data that support the findings of this study are available from the corresponding author upon reasonable request.

**APPENDIX: MASS TRANSFER MODEL**

To accurately capture the phase transition during the cavitation process, the mass conservation equation of the vapor–liquid flow is expressed as follows:

$$\frac{\partial \rho_l \alpha_l}{\partial t} + \frac{\partial \rho_l \alpha_l \bar{u}_i}{\partial x_i} = R^c - R^e, \tag{A1}$$

$$\frac{\partial \rho_v \alpha_v}{\partial t} + \frac{\partial \rho_v \alpha_v \bar{u}_i}{\partial x_i} = R^e - R^c, \tag{A2}$$

where  $\dot{m}$  is the mass conversion rate of the cavitation phase transition. To facilitate the solution of the content equations, Eqs. (A1) and (A2) are expanded into the transport equation form of the volume fraction

$$\frac{\partial \alpha_l}{\partial t} + \frac{\partial \alpha_l \bar{u}_i}{\partial x_i} = -\frac{\alpha_l D \rho_l}{\rho_l Dt} + \frac{R^c - R^e}{\rho_l}, \tag{A3}$$

$$\frac{\partial \alpha_v}{\partial t} + \frac{\partial \alpha_v \bar{u}_i}{\partial x_i} = -\frac{\alpha_v D \rho_v}{\rho_v Dt} - \frac{R^c - R^e}{\rho_v}, \tag{A4}$$

where  $\frac{D}{Dt}$  represents the material derivative and the volume fraction satisfies  $\alpha_l + \alpha_v = 1.0$ . Therefore, the constraint equation is obtained by adding Eqs. (A3) to (A4)

$$\frac{\partial \bar{u}_i}{\partial x_i} = -\frac{\alpha_l D \rho_l}{\rho_l Dt} - \frac{\alpha_v D \rho_v}{\rho_v Dt} + \left(\frac{1}{\rho_l} - \frac{1}{\rho_v}\right)(R^c - R^e). \tag{A5}$$

In the incompressible flow,  $\frac{\alpha_l D \rho_l}{\rho_l Dt} = \frac{\alpha_v D \rho_v}{\rho_v Dt} = 0$ , and Eq. (A5) can therefore be expressed as  $\frac{\partial \bar{u}_i}{\partial x_i} = \left(\frac{1}{\rho_l} - \frac{1}{\rho_v}\right)(R^c - R^e)$ , denoted as  $S_p$

$$S_p = \frac{\partial \bar{u}_i}{\partial x_i} = \left(\frac{1}{\rho_l} - \frac{1}{\rho_v}\right)(R^c - R^e). \tag{A6}$$

**REFERENCES**

- <sup>1</sup>M. R. Pendar and E. Roohi, “Investigation of cavitation around 3D hemispherical head-form body and conical cavitators using different turbulence and cavitation models,” *Ocean Eng.* **112**, 287–306 (2016).
- <sup>2</sup>M. H. Bappy, P. M. Carrica, A. Vela-Martín, L. S. Freire, and G. C. Buscaglia, “Pressure statistics of gas nuclei in homogeneous isotropic turbulence with an application to cavitation inception,” *Phys. Fluids* **32**, 095107 (2020).
- <sup>3</sup>C. Yu, Y. W. Wang, C. G. Huang, T. Z. Du, C. Xu, and J. Huang, “Experimental and numerical investigation on cloud cavitating flow around an axisymmetric projectile near the wall with emphasis on the analysis of local cavity shedding,” *Ocean Eng.* **140**, 377–387 (2017).
- <sup>4</sup>M. H. Bappy, P. M. Carrica, J. J. Li, J. E. Martin, A. Vela-Martín, L. S. Freire, and G. C. Buscaglia, “A sub-grid scale cavitation inception model,” *Phys. Fluids* **34**, 033308 (2022).
- <sup>5</sup>W. Q. Chen and J. Xu, “A linear theoretical model of cavitation flow past a multihydrofoil system with a finite number of foils,” *Appl. Math. Modell.* **77**, 1691–1703 (2020).
- <sup>6</sup>A. Papoutsakis, A. Koukouvinis, and M. Gavaises, “Solution of cavitating compressible flows using discontinuous Galerkin discretisation,” *J. Comput. Phys.* **410**, 109377 (2020).
- <sup>7</sup>A. Yu, X. C. Wang, Q. H. Tang, and D. Q. Zhou, “Large eddy simulation of the periodic cavity evolution and the turbulence characteristics around a delft twist-11 hydrofoil,” *J. Turbul.* **21**, 386–405 (2020).
- <sup>8</sup>V. H. Arakeri and A. J. Acosta, “Viscous effects in the inception of cavitation on axisymmetric bodies,” *J. Fluids Eng.* **95**, 519–527 (1973).
- <sup>9</sup>C. O. Iyer and S. L. Ceccio, “The influence of developed cavitation on the flow of a turbulent shear layer,” *Phys. Fluids* **14**, 3414–3431 (2002).
- <sup>10</sup>P. A. Lush and S. R. Skipp, “High speed cine observations of cavitating flow in a duct,” *Int. J. Heat Fluid Flow* **7**, 283–290 (1986).

- <sup>11</sup>B. Huang, G. Wang, Y. U. Zhiyi, and S. Shi, “Detached-eddy simulation for time-dependent turbulent cavitating flows,” *Chin. J. Mech. Eng.* **25**, 484–490 (2012).
- <sup>12</sup>B. Ji, X. Luo, Y. Wu, X. Peng, and Y. Duan, “Numerical analysis of unsteady cavitating turbulent flow and shedding horse-shoe vortex structure around a twisted hydrofoil,” *Int. J. Multiphase Flow* **51**, 33–43 (2013).
- <sup>13</sup>Y. W. Wang, C. G. Huang, X. Fang, X. X. Yu, X. C. Wu, and T. Z. Du, “Cloud cavitating flow over a submerged axisymmetric projectile and comparison between two-dimensional RANS and three-dimensional large-eddy simulation methods,” *J. Fluids Eng.* **138**, 061102 (2016).
- <sup>14</sup>G. Wang and M. Ostoja-Starzewski, “Large eddy simulation of a sheet/cloud cavitation on a NACA0015 hydrofoil,” *Appl. Math. Modell.* **31**, 417–447 (2007).
- <sup>15</sup>B. Ji, X. W. Luo, R. Arndt, X. Peng, and Y. Wu, “Large eddy simulation and theoretical investigations of the transient cavitating vortical flow structure around a NACA66 hydrofoil,” *Int. J. Multiphase Flow* **68**, 121–134 (2015).
- <sup>16</sup>X. C. Wu, Y. W. Wang, and C. G. Huang, “Effect of mesh resolution on large eddy simulation of cloud cavitating flow around a three dimensional twisted hydrofoil,” *Eur. J. Mech. -B/Fluids* **55**, 229–240 (2016).
- <sup>17</sup>A. Yu, W. J. Feng, and Q. H. Tang, “Numerical study on the pulsating energy evolution in the cavitating flow around a mini cascade,” *Phys. Fluids* **34**, 123308 (2022).
- <sup>18</sup>B. Ji, H. Y. Cheng, B. Huang, X. W. Luo, X. X. Peng, and X. P. Long, “Research progresses and prospects of unsteady hydrodynamics characteristics for cavitation,” *Adv. Mech.* **49**, 201906 (2019).
- <sup>19</sup>B. Huang, G. Y. Wang, and Y. Zhao, “Numerical simulation unsteady cloud cavitating flow with a filter-based density correction model,” *J. Hydrodyn., Ser. B* **26**, 26–36 (2014).
- <sup>20</sup>J. Y. Wu, G. Y. Wang, and W. Shyy, “Time-dependent turbulent cavitating flow computations with interfacial transport and filter-based models,” *Int. J. Numer. Methods Fluids* **49**, 739–761 (2005).
- <sup>21</sup>A. Gnanaskandan and K. Mahesh, “A numerical method to simulate turbulent cavitating flows,” *Int. J. Multiphase Flow* **70**, 22–34 (2015).
- <sup>22</sup>Q. Wu, B. Huang, G. Wang, and Y. Gao, “Experimental and numerical investigation of hydroelastic response of a flexible hydrofoil in cavitating flow,” *Int. J. Multiphase Flow* **74**, 19–33 (2015).
- <sup>23</sup>T. Z. Du, Y. W. Wang, L. J. Liao, and C. G. Huang, “A numerical model for the evolution of internal structure of cavitation cloud,” *Phys. Fluids* **28**, 077103–077120 (2016).
- <sup>24</sup>J. Capececlatro, O. Desjardins, and R. O. Fox, “On fluid–particle dynamics in fully developed cluster-induced turbulence,” *J. Fluid Mech.* **780**, 578–635 (2015).
- <sup>25</sup>S. Vahaji, J. Han, S. C. P. Cheung, G. H. Yeoh, and J. Y. Tu, “Numerical investigation on the bubble size distribution around NACA0015 hydrofoil,” *Ocean Eng.* **172**, 59–71 (2019).
- <sup>26</sup>S. Beetham and J. Capececlatro, “Biomass pyrolysis in fully-developed turbulent riser flow,” *Renewable Energy* **140**, 751–760 (2019).
- <sup>27</sup>O. Coutier-Delgosha, R. F. Patella, and J. L. Reboud, “Evaluation of the turbulence model influence on the numerical simulations of unsteady cavitation,” *J. Fluids Eng.-Trans. ASME* **125**, 38–45 (2003).
- <sup>28</sup>X. Li, G. Wang, Z. Yu, and S. Wei, “Multiphase fluid dynamics and transport processes of low capillary number cavitating flows,” *Acta Mech. Sin.* **25**, 161–172 (2009).
- <sup>29</sup>Y. W. Wang, C. G. Huang, X. Fang, X. C. Wu, and T. Z. Du, “On the internal collapse phenomenon at the closure of cavitation bubbles in a deceleration process of underwater vertical launching,” *Appl. Ocean Res.* **56**, 157–165 (2016).
- <sup>30</sup>H. Xiao and P. Cinnella, “Quantification of model uncertainty in RANS simulations: A review,” *Prog. Aerosp. Sci.* **108**, 1–31 (2019).
- <sup>31</sup>S. Taghizadeh, F. D. Witherden, and S. S. Girimaji, “Turbulence closure modeling with data-driven techniques: Physical compatibility and consistency considerations,” *New J. Phys.* **22**, 093023 (2020).
- <sup>32</sup>R. K. Tripathy and I. Bilionis, “Deep UQ: Learning deep neural network surrogate models for high dimensional uncertainty quantification,” *J. Comput. Phys.* **375**, 565–588 (2018).
- <sup>33</sup>S. Taghizadeh, F. D. Witherden, Y. A. Hassan, and S. S. Girimaji, “Turbulence closure modeling with data-driven techniques: Investigation of generalizable deep neural networks,” *Phys. Fluids* **33**, 115132 (2021).
- <sup>34</sup>X. Jin, P. Cheng, W. L. Chen, and H. Li, “Prediction model of velocity field around circular cylinder over various Reynolds numbers by fusion convolutional neural networks based on pressure on the cylinder,” *Phys. Fluids* **30**, 047105 (2018).
- <sup>35</sup>Y. H. Zhu and N. Zabaras, “Bayesian deep convolutional encoder–decoder networks for surrogate modeling and uncertainty quantification,” *J. Comput. Phys.* **366**, 415–447 (2018).
- <sup>36</sup>S. R. Ye, Z. Zhang, X. D. Song, Y. W. Wang, and C. G. Huang, “A flow feature detection method for modeling pressure distribution around a cylinder in non-uniform flows by using a convolutional neural network,” *Sci. Rep.* **10**, 4459 (2020).
- <sup>37</sup>Y. H. Yin, Y. Pu, Y. F. Zhang, H. X. Chen, and S. Fu, “Feature selection and processing of turbulence modeling based on an artificial neural network,” *Phys. Fluids* **32**, 105117 (2020).
- <sup>38</sup>M. C. Yang and Z. X. Xiao, “Improving the  $k - \omega - \gamma - A_r$  transition model by the field inversion and machine learning framework,” *Phys. Fluids* **32**, 064101 (2020).
- <sup>39</sup>K. Duraisamy, G. Iaccarino, and H. Xiao, “Turbulence modeling in the age of data,” *Annu. Rev. Fluid Mech.* **51**, 357–377 (2019).
- <sup>40</sup>N. Geneva and N. Zabaras, “Quantifying model form uncertainty in Reynolds-averaged turbulence models with Bayesian deep neural networks,” *J. Comput. Phys.* **383**, 125–147 (2019).
- <sup>41</sup>H. Xiao, J. L. Wu, J. X. Wang, R. Sun, and C. J. Roy, “Quantifying and reducing model-form uncertainties in Reynolds-averaged Navier–Stokes simulations: A data-driven, physics-informed Bayesian approach,” *J. Comput. Phys.* **324**, 115–136 (2016).
- <sup>42</sup>J. X. Wang, J. L. Wu, and H. Xiao, “Physics-informed machine learning approach for reconstructing Reynolds stress modeling discrepancies based on DNS data,” *Phys. Rev. Fluids* **2**, 034603 (2017).
- <sup>43</sup>J. Ling and J. Templeton, “Evaluation of machine learning algorithms for prediction of regions of high Reynolds averaged Navier Stokes uncertainty,” *Phys. Fluids* **27**, 085103 (2015).
- <sup>44</sup>A. P. Singh, S. Medida, and K. Duraisamy, “Machine-learning-augmented predictive modeling of turbulent separated flows over airfoils,” *AIAA J.* **55**, 2215–2227 (2017).
- <sup>45</sup>J. Ling, A. Kurzawski, and J. Templeton, “Reynolds averaged turbulence modeling using deep neural networks with embedded invariance,” *J. Fluid Mech.* **807**, 155–166 (2016).
- <sup>46</sup>Z. Zhang, X. D. Song, S. R. Ye, Y. W. Wang, C. G. Huang, Y. R. An, and Y. S. Chen, “Application of deep learning method to Reynolds stress models of channel flow based on reduced-order modeling of DNS data,” *J. Hydrodyn.* **31**, 58–65 (2019).
- <sup>47</sup>F. Köhler, J. Munz, and M. Schäfer, “Data-driven augmentation of RANS turbulence models for improved prediction of separation in wall-bounded flows,” AIAA Paper No. 2020-1586, 2020.
- <sup>48</sup>B. Parmar, E. Peters, K. E. Jansen, A. Doostan, and J. A. Evans, “Generalized non-linear eddy viscosity models for data-assisted Reynolds stress closure,” AIAA Paper No. 2020-0351, 2020.
- <sup>49</sup>H. Xiao, J. L. Wu, S. Laizet, and L. Duan, “Flows over periodic hills of parameterized geometries: A dataset for data-driven turbulence modeling from direct simulations,” *Comput. Fluids* **200**, 104431 (2020).
- <sup>50</sup>J. Weatheritt and R. Sandberg, “A novel evolutionary algorithm applied to algebraic modifications of the RANS stress–strain relationship,” *J. Comput. Phys.* **325**, 22–37 (2016).
- <sup>51</sup>H. Qi, X. Li, and C. Yu, “Subgrid-scale model based on the vorticity gradient tensor for rotating turbulent flows,” *Acta Mech. Sin.* **36**, 692–700 (2020).
- <sup>52</sup>J. Wu, H. Xiao, and E. G. Paterson, “Physics-informed machine learning approach for augmenting turbulence models: A comprehensive framework,” *Phys. Rev. Fluids* **3**, 074602 (2018).
- <sup>53</sup>J. Wu, H. Xiao, R. Sun, and Q. Wang, “Reynolds-averaged Navier–Stokes equations with explicit data-driven Reynolds stress closure can be ill-conditioned,” *J. Fluid Mech.* **869**, 553–586 (2019).
- <sup>54</sup>Z. Zhang, S. Ye, B. Yin, X. Song, W. Yiwei, H. Chenguang, and C. Yaosong, “A semi-implicit discrepancy model of Reynolds stress in a higher-order tensor basis framework for Reynolds-averaged Navier–Stokes simulations,” *AIP Adv.* **11**, 045025 (2021).

- <sup>55</sup>F. Nicoud and F. Ducros, "Subgrid-scale stress modelling based on the square of the velocity gradient tensor," *Flow Turbul. Combust.* **62**, 183–200 (1999).
- <sup>56</sup>L. Davidson, *Fluid Mechanics, Turbulent Flow and Turbulence Modeling* (Chalmers University of Technology, Goteborg, Sweden, 2018).
- <sup>57</sup>F. G. Schmitt, "About Boussinesq's turbulent viscosity hypothesis: Historical remarks and a direct evaluation of its validity," *C.R. Méc.* **335**, 617–627 (2007).
- <sup>58</sup>P. J. Zwart, A. G. Gerber, and T. Belamri, "A two-phase flow model for predicting cavitation dynamics," in Proceedings of the 5th International Conference on Multiphase Flow (2001).
- <sup>59</sup>S. B. Pope, "A more general effective-viscosity hypothesis," *J. Fluid Mech.* **72**, 331–340 (1975).
- <sup>60</sup>W. Wróblewski, K. Bochon, M. Majkut, E. H. Malekshah, K. Rusin, and M. Strozik, "An experimental/numerical assessment over the influence of the dissolved air on the instantaneous characteristics/shedding frequency of cavitating flow," *Ocean Eng.* **240**, 109960 (2021).
- <sup>61</sup>R. Deshpande, C. M. De Silva, M. Lee, J. P. Monty, and I. Marusic, "Data-driven enhancement of coherent structure-based models for predicting instantaneous wall turbulence," *Int. J. Heat Fluid Flow* **92**, 108879 (2021).
- <sup>62</sup>Z. X. Ma, J. Yu, and R. Y. Xiao, "Data-driven reduced order modeling for parameterized time-dependent flow problems," *Phys. Fluids* **34**, 075109 (2022).
- <sup>63</sup>A. L. Maas, A. Y. Hannun, and A. Y. Ng, "Rectifier nonlinearities improve neural network acoustic models," in *Proceedings of the International Conference on Machine Learning (ICML)* (Association for Computing Machinery, New York, NY, 2013).
- <sup>64</sup>H. Cheng, X. Long, B. Ji, X. Peng, and M. Farhat, "LES investigation of the influence of cavitation on flow patterns in a confined tip-leakage flow," *Ocean Eng.* **186**, 106115 (2019).
- <sup>65</sup>H. Ganesh, S. A. Makiharju, and S. L. Ceccio, "Bubbly shock propagation as a mechanism for sheet-to-cloud transition of partial cavities," *J. Fluid Mech.* **802**, 37–78 (2016).
- <sup>66</sup>M. Bhatt and K. Mahesh, "Numerical investigation of partial cavitation regimes over a wedge using large eddy simulation," *Int. J. Multiphase Flow* **122**, 103155 (2019).
- <sup>67</sup>J. B. Leroux, J. A. Astolfi, and J. Y. Billard, "An experimental study of unsteady partial cavitation," *J. Fluids Eng.* **126**, 94–101 (2004).
- <sup>68</sup>B. Huang, G. Y. Wang, Y. Zhao, and Q. Wu, "Physical and numerical investigation on transient cavitating flows," *Sci. China Technol. Sci.* **56**, 2207–2218 (2013).
- <sup>69</sup>G. Wang, I. Senocak, and S. Wei, "Dynamics of attached turbulent cavitating flows," *Prog. Aerosp. Sci.* **37**, 551–581 (2001).